

# Embryo impacts and gas giant mergers II: Diversity of Hot Jupiters' internal structure

Shang-Fei Liu<sup>1,2</sup>, Craig B. Agnor<sup>3</sup>, D. N. C. Lin<sup>1,4,5</sup> and Shu-Lin Li<sup>1,6</sup>

<sup>1</sup> *Kavli Institute for Astronomy and Astrophysics and Department of Astronomy, Peking University, Beijing 100871, China; E-mail: liushangfei@pku.edu.cn*

<sup>2</sup> *Department of Earth and Planetary Sciences, University of California, Santa Cruz, CA 95064, USA*

<sup>3</sup> *Astronomy Unit, School of Physics and Astronomy, Queen Mary University of London, United Kingdom*

<sup>4</sup> *Department of Astronomy and Astrophysics, University of California, Santa Cruz, CA 95064, USA*

<sup>5</sup> *Institute for Advanced Studies, Tsinghua University, Beijing 100084, China*

<sup>6</sup> *National Astronomical Observatory of China, Chinese Academy of Sciences Beijing 100012, China*

3 October 2018

## ABSTRACT

We consider the origin of compact, short-period, Jupiter-mass planets. We propose that their diverse structure is caused by giant impacts of embryos and super-Earths or mergers with other gas giants during the formation and evolution of these hot Jupiters. Through a series of numerical simulations, we show that typical head-on collisions generally lead to total coalescence of impinging gas giants. Although extremely energetic collisions can disintegrate the envelope of gas giants, these events seldom occur. During oblique and moderately energetic collisions, the merger products retain higher fraction of the colliders' cores than their envelopes. They can also deposit considerable amount of spin angular momentum to the gas giants and desynchronize their spins from their orbital mean motion. We find that the oblateness of gas giants can be used to infer the impact history. Subsequent dissipation of stellar tide inside the planets' envelope can lead to runaway inflation and potentially a substantial loss of gas through Roche-lobe overflow. The impact of super-Earths on parabolic orbits can also enlarge gas giant planets' envelope and elevates their tidal dissipation rate over  $\sim 100$  Myr time scale. Since giant impacts occur stochastically with a range of impactor sizes and energies, their diverse outcomes may account for the dispersion in the mass-radius relationship of hot Jupiters.

**Key words:** Extrasolar planets; planetary formation; planetary dynamics; planetary structure

## 1 INTRODUCTION

In the conventional sequential accretion hypothesis (SAH), gas giant planets acquire critical-mass ( $\sim 10M_{\oplus}$ ) cores prior to the onset of efficient gas accretion (Pollack et al. 1996; Ida & Lin 2004). This scenario can account for many observational properties of Jupiter, Saturn, and extra-solar planets (Schlaufman, Lin & Ida 2009). However, the observed large dispersion in the internal structures of gas giant planets was not anticipated, even taking into account the fact that the assumptions they made to get this critical value may not be universal.

In the first paper of this series (Li, Agnor & Lin 2010, hereafter Paper I), we attribute the dichotomy between the mass of Jupiter and Saturn's cores to giant impacts by embryos and mergers of gas giants during their formation and early dynamical evolution. Using two numerical methods, we simulated a series of models with parabolic collisions and show that these collisions generally lead to the accretion of embryos and coalescence of gas giants. We also

show that massive super-Earth impactors can survive passage deep into the envelope of a gas giant and release energy near the core. This may drive intense convective motion in the planet and core erosion. In contrast, sub-Earths embryos disintegrate higher in the gaseous envelope and their fragments will dissolve in the envelope and contribute to a heavy element enrichment.

Transit surveys suggest that there is a remarkable diversity in hot Jupiters' radii. Extrasolar planets with masses comparable to Jupiter range in size by a factor of more than two (Figure 1). Some of these planets (*e.g.* HD 209458 b) have Jupiter mass ( $M_J$ ) but more than 30 % larger radius. Several planets (such as Corot 8 b and WASP 29 b) have masses comparable to Saturn, but radii  $R_p$  that are much smaller than Saturn's. These compact planets may require the presence of massive cores (*e.g.* up to  $70M_{\oplus}$  core is needed for HD 149026 b). The main focus of this paper is to apply the giant impact and merger scenario (GIMs) to account for large dispersion in hot Jupiters' radii.

In order to construct this scenario, we briefly cite observa-

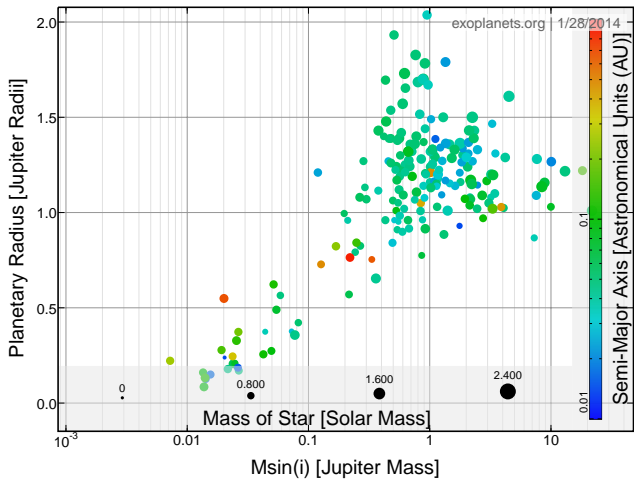


**Figure 1.** The mass-radius distribution of transiting exoplanets color coded with their semi-major axes. The size of symbols indicate masses of their host stars. Data were taken from the Exoplanet Data Explorer (<http://exoplanets.org/>) on Jan. 28, 2014.

tional evidence for the structural and atmospheric diversity of hot Jupiters. Through a brief recapitulation of their origin, we present arguments in §2, to suggest that GIMs occur frequently during and after orbital migration to the proximity of their host stars. In §3, we used two complementary approaches: a Lagrangian smoothed particle hydrodynamics (SPH) code, and the Eulerian adaptive mesh hydrodynamics code FLASH (Fryxell et al. 2000) to simulate both head-on and oblique collisions between a Saturn-mass giant planet and a  $10-M_{\oplus}$  or  $25-M_{\oplus}$  embryo. These models extend the previous models to the high energy limit. We show that most hyperbolic oblique encounters deposit spin angular momentum to gas giants. Highly energetic collisions can directly lead to the substantial loss of envelope gas beyond their Roche radii. SPH and FLASH simulations of merger between two Saturn-like gas giants are also presented.

In order to expand the dynamical range for density and investigate the long term evolution in our simulated models, we adopted, in paper I, a one-dimensional Lagrangian hydrodynamic (LHD) scheme which can be used to study the effect of tidal interaction of inflated merger products with the host stars. With LHD, we show in §4, the energy released from modest giant impacts can also induce the expansion of the gas giants’ envelope. Subsequent dissipation of stellar tidal perturbation in the gas giants may lead to runaway inflation. Since gas in the envelope is preferentially lost, these encounters lead to the enhancement of the planet’s metallicity and asymptotic compact size. Finally, we summarize our results and discuss their observational implications in §5.

## 2 GIANT IMPACT HISTORY OF CLOSE-IN GAS GIANTS.

In paper I, we discuss the possibility of GIMs for long-period gas giants in the proximity of the birth place as an avenue for the enrichment of their envelope and a cause for structural diversity between Jupiter and Saturn. It is difficult to directly detect the metallicity and accurately determine the internal structure of extrasolar planets. However, if the metallicity ( $[Fe/H]$ ), envelope and core masses

( $M_{\text{env}}$  and  $M_{\text{core}}$ ), the orbit and spin state of any planet are known, it is possible to construct its contraction sequence, taking into account stellar irradiation and tidal dissipation (Bodenheimer, Lin & Mardling 2001; Bodenheimer, Laughlin & Lin 2003). Although the interior structure of extrasolar gas giant planets remains uncertain and is an area of active research, in this work we simply ignore complicating factors, assume a core-envelope structure and assume that the core of any planet can be inferred from its measured radius ( $R_p$ ) and the age of its host star ( $\tau_*$ ).

As of this writing there are more than 200 transiting gas giants with measured masses  $M_p$  and radii  $R_p$ <sup>1</sup>. Due to an observational selection effect, most of the known transiting gas giant planets are close-in planets known as hot Jupiters with periods and masses in the range of a few days and Jupiter mass respectively. The diversity in the value of their measured radii  $R_p$  and densities motivated us to invoke the GIM scenario.

### 2.1 Possible causes for inflated hot Jupiters.

Most of the transiting hot Jupiters have  $R_p$ ’s consistent with those expected from models constructed for their  $M_p$  including cores with  $M_{\text{core}} \sim 10 - 20 M_{\oplus}$ . However, there are several transiting planets, such as HD 209458b, Trés-4 (Mandushev et al. 2007), and WASP-12b (Li et al. 2010) which have observationally inferred radii much larger than that of Jupiter ( $R_J$ ) even though their mass is comparable to that of Jupiter. For the special class of inflated hot Jupiters, suggestions for their unusually low densities include:

- 1) the thermal contraction of these planets is suppressed by the stellar irradiation (Burrows et al. 2000, 2004),
- 2) they are inflated by additional heating sources such as the dissipation due to the ongoing stellar tidal perturbation (Bodenheimer, Lin & Mardling 2001),
- 3) irradiation-driven circulation (Showman & Guillot 2002), or associated Ohmic dissipation (Batygin & Stevenson 2010; Wu & Lithwick 2013)
- 4) the sedimentation of heavy elements (Baraffe, Chabrier & Barman 2008).

Most of these propositions have some difficulties in accounting for the difference between the exceptions and the other “normal” gas giant planets. Here we suggest another scenario. Following Paper I, we suggest that the energy dissipation during GIM’s and the tidal dissipation thereafter may be adequate to inflate some gas giant planets. The stochastic nature of GIM’s provides a possible explanation for the wide dispersion  $M_p - R_p$  distribution of hot Jupiters.

### 2.2 Hot Jupiters with massive cores or most metallic compositions.

In paper I we showed that GIM’s may lead to transitory planetary inflation. Merger events of two or more gas giants and multiple impacts of earth-mass embryos may also lead to the formation of massive cores and the heavy metallicity contamination of planetary envelopes. In this paper, we explore the possibility that giant impacts and mergers may produce mature, compact, hot Jupiters.

HD 149026 b has an observed radius of  $R_p = 0.73R_J$  and the mass of Saturn (Sato et al. 2005). Structural analysis indicates that

<sup>1</sup> see, e.g., <http://exoplanets.org/>.

more than half ( $\sim 70 M_{\oplus}$ ) of its total mass may be contained within a core of heavy elements (Sato et al. 2005). Later models suggest that it is also possible for heavy elements to distribute throughout the interior of the planet (Ikoma et al. 2006; Baraffe, Chabrier & Barman 2008). The extraordinary compact radius of HD 149026 b poses a challenge to both gravitational instability and sequential accretion hypothesis (SAH) for gas giant planet formation.

The required metallicity of HD 149026 b is more than an order of magnitude larger than that of its star (which has a mass  $M_* = 1.3 M_{\odot}$  and metallicity  $[\text{Fe}/\text{H}] = 0.36$ ). If this planet formed through gravitational instability (Boss 1997), this heavy elemental concentration would require either an enormous loss of its original gaseous envelope or an extensive acquisition of heavy elemental material through the post-formation accretion of solid planetesimals and proto-planetary embryos.

If this planet acquired its present-day structure through core accretion (Pollack et al. 1996) such a massive core would be attainable in a gas-rich environment beyond the snow-line provided it can avoid initial dynamical isolation. In principle, at several AU's from its host star, the isolation mass  $M_{\text{iso}}$  of proto-planetary solid embryos can reach this massive level provided the local surface density of heavy elements  $\Sigma_g$  is more than an order of magnitude larger than that inferred from the MMN model. In the disk around a host star with solar metallicity, the inferred  $\Sigma_g$  would render the augmented disk to be gravitationally unstable.

However, if the core-building material is able to congregate in some confined locations such as the snow line, solid embryos with very large  $M_{\text{iso}}$  would be attainable in a gravitational stable disk, prior to the accretion of a relatively massive envelope. An additional requirement is that the planetesimal accretion rate must exceed the gas accretion rate until the core has already acquired most of its present-day mass. With its massive core, this requirement may be difficult to accomplish for HD 149026 b because the heat loss is efficient and the gas accretion rate are likely to be large around any cores with  $M_{\text{core}} > 20M_{\oplus}$ .

During the phase of gas accretion, the protoplanets' feeding zones expand with their masses. Early models for core accretion are constructed under the assumption that all embryos in the expanding feeding zone are accreted by the growing protoplanet (Pollack et al. 1996). However, these embryos have a tendency to migrate away from the protoplanets and form gaps around them during their initial phase of modest gas accretion. Only when the gas giants rapidly accrete massive envelopes do the orbits of their nearby residual embryos become destabilized and a modest fraction of the orbit-crossing embryos would merge with them (Zhou & Lin 2007; Shiraishi & Ida 2008). However, the total mass of HD 149026 b's gaseous envelope is smaller than that contain in the heavy elements.

The above discussion indicates that the formation of some isolated gas giants with massive cores cannot be ruled out *a priori*. But these compact planets are apparently exceptions rather than the general rule. Around a host star OGLE-TR-132, a transiting planet has been found with similar  $M_p$  and  $a$  as those of HD 149026 b. Despite the nearly identical  $[\text{Fe}/\text{H}]$  for both host stars, OGLE-TR-132 b has a radius nearly twice that of HD 149026 b (Gillon et al. 2007). Presumably, OGLE-TR-132 b has a much smaller core mass than HD 149026 b. The large discrepancy between these two same-mass planets around similar host stars again points to stochastic origins of their internal structures. The large dispersion in the average density of known gas giants (Figure 1) is further evidence of this structure diversity.

Here we adopt the proposition and examine the possibility that the massive core of compact planets such as HD 149026 b are the byproduct of one or more giant impacts and mergers (Sato et al. 2005; Ikoma et al. 2006) in close proximity to its host star. Whereas those planets with unusually large radii may have been struck recently (within the last  $\sim 100$  Myr) by modest-mass embryos (with masses up to  $\sim M_{\oplus}$ ), the impactors for this compact planet are either another gas giant or very massive (up to  $\sim 10\text{--}20M_{\oplus}$ ) embryos. We also suggest that these collisions occur so long ( $> 1$  Gyr) ago that the internal structure of this planet has had adequate time to readjust to a new thermal equilibrium.

### 2.3 Availabilities of residual embryos as potential impactors of emerging gas giants

We first consider the possibility of giant impacts during the formation of gas giants. In typical disks around classical T Tauri stars, super-Earth embryos are not sufficiently massive to open gaps (Lin, Papaloizou & Kley 1993). Nonetheless, they tidally interact with the disk and undergo type I migration (Goldreich & Tremaine 1980; Ward 1984, 1997). Their migration time scale and direction are determined by the sum of the planets' corotation and Lindblad torques on the disk and by the disk structure (Paardekooper, Baruteau & Kley 2011). There is a tendency for the super-Earth embryos to converge toward some trapping radii where their enhanced surface density promotes the embryos' oligarchic growth and the emergence of cores with sufficient mass to initiate efficient gas accretion. As they rapidly gain mass, emerging protoplanets destabilize the orbits of neighboring residual sub-critical embryos (Zhou & Lin 2007). Some of these embryos collide with the protoplanets (see paper I).

With sufficient masses, proto gas giants open gaps. In extended protostellar disks, gas giants form interior to the half mass radius of the disk and undergo inward type II migration and become hot Jupiters (Lin, Bodenheimer & Richardson 1996). Along the way, the migrating gas giants capture residual embryos in their sweeping mean motion resonances (Zhou et al. 2005).

Although the relatively low-mass embryos have not migrated extensively on their own, they are being shepherded to spiral toward their stars with the migrating gas giants (cf Yu & Tremaine 2001). This snow-plough effect has led to the formation of the resonant gas giant planets systems around 55 Cnc and GJ 876 (Lee & Peale 2002). This process can excite embryos' eccentricity, lead to orbit crossing, and enhance the possibility of giant impacts (Zhou et al. 2005; Fogg & Nelson 2007; Mandell, Raymond & Sigurdsson 2007).

Many gas giants are members of multiple planet systems. During the stage when two or more gas giants capture each other into their mutual mean motion resonances (such as those around GJ 876 and 55 Cnc) or enter into secular resonances (such as those around Ups And), their apsidal precession frequencies change greatly (Murray & Holman 1999). The location of their secular resonances also sweeps over extensively wide regions during the depletion of the solar nebula (Ward 1981), or during later gas-free planetesimal-driven or instability-driven giant planet migration (Agnor & Lin 2012). These resonances may excite eccentricities of super-Earths and result in giant impacts with gas giants.

Ketchum, Adams & Bloch (2011) studied an alternative scenario, in which super-Earths form and migrate inward after hot Jupiters complete inward migration and reside inside the inner edge

of the disk. They found those super-Earths have a great chance to collide with the inner gas giant if the eccentricity damping is not efficient.

#### 2.4 Supply of potential impactors to hot Jupiters during the epoch of disk depletion.

The trapping radius where super Earths converge depends the surface density and temperature distribution in the disk. These quantities are also functions of disks' accretion rate, effective viscosity, and stellar luminosity (Garau & Lin 2007). In models with a standard  $\alpha$  prescription, super Earths' trapping radius is located at the transition between the inner disk which is heated by viscous dissipation and the outer disk where stellar irradiation provides the dominant thermal energy (Kretke & Lin 2012). During the advanced stage of disk evolution when accretion diminishes with gas depletion, the trapping radius contracts and the magnetosphere truncation radius expands. Through this process, super Earths may accumulate in the proximity of their host stars.

On the observational front, radial velocity and transit surveys indicate that solar-type stars bear super-Earths, with mass and period up to  $\sim 20 M_{\oplus}$  and a few months, are more common than those with Jupiter-mass gas giants. Radial velocity survey with HARPS reports that it may be in the range 39-58%, though only a few of these claims have actually been published (Mayor et al 2009, Udry private communication). Although the eta-of-Earth survey (Howard et al. 2010) suggests a lower fraction of stars with super-Earths, it nonetheless indicates that the frequency of stars with short-period planets is a rapidly decreasing function of planet mass. The common existence of super-Earths is also suggested by many detections in the Kepler transit survey. In many cases, these super-Earths are members of multiple-planet systems in which migration and dynamical interaction most likely have influenced their formation and evolution (Papaloizou & Terquem 2010).

After the disk depletion, mutual secular perturbation between co-existing hot Jupiters and close-in super Earths leads to eccentricity excitation and eventually dynamical instability. Numerical simulations (Zhou, Lin & Sun 2007) indicate that multiple planets, with equal masses  $M_p$  and a normalized separation  $k_0 = \Delta a/R_H$  where  $a$ ,  $\Delta a$ , and  $R_H = a(2M_p/3M_*)^{1/3}$  are the semi major axis, separation, and Hill radius, undergo orbit crossing on a time scale

$$\log(T_c/P_k) \simeq -5 + 2.2k_0, \quad (1)$$

where  $P_k$  is the mean orbital period.

In §2 Paper I, we have indicated that self gravity of protostellar disks introduces precession in the eccentric orbits of gas giants. Secular resonances occur in regions of disks where precession rates due to the gravitational perturbation of these planets matches with their precession rate due to the disk potential. As  $\Sigma_g$  decreases, these secular resonances sweep across them. Passage of the secular resonances excites the eccentricity of residual planets and super-Earths (Ward 1981; Nagasawa, Lin & Thommes 2005) including those with short periods (such as *v* And b and  $\mu$  Ari b (Nagasawa & Lin 2005; Zhou et al. 2005)). This process can also lead to orbit crossings which destabilize multiple planet systems and induce potential giant impact events(Thommes, Nagasawa & Lin 2008).

#### 2.5 Hot Jupiters' potential impactors around mature stars

In compact systems of multiple hot Jupiters and close-in super-Earths the crossing time scale may be lengthened by the stabilizing contributions of relativistic precession and internal tidal dissipation (Mardling & Lin 2004; Mardling 2007; Terquem & Papaloizou 2007). However, these planets undergo further decay(Novak, Lai & Lin 2003; Lee, Fabrycky & Lin 2013) which may eventually lead to dynamical instabilities, orbit crossing, and eventually cohesive collisions (Lin & Ida 1997).

Compact systems of long-period planets also undergo orbit crossing, on the time scale of  $T_c$  and excite each other eccentricities (Weidenschilling & Marzari 1996; Rasio & Ford 1996; Lin & Ida 1997; Zhou, Lin & Sun 2007; Jurić & Tremaine 2008; Chatterjee et al. 2008). Known gas giants with periods longer than 1-2 weeks have nearly uniform eccentricity distribution ranging from zero to nearly unity. Subsequent close encounters, secular chaos, Kozai resonances, and external perturbations (Wu & Murray 2003; Wu, Murray & Ramsahai 2007), (Laughlin & Adams 1998; Adams & Laughlin 2001; Spurzem et al. 2009; Nagasawa & Ida 2011; Wu & Lithwick 2011) may drive distant planets to highly eccentric orbits where they may begin nearly parabolic close encounters with their host stars. It has been suggested that a significant fraction of hot Jupiters, especially those with high obliquities, may be scattered to the proximity of their host stars with follow-up tidal circularization of their orbits (Faber, Rasio & Willems 2005; Fabrycky & Tremaine 2007; Narita et al. 2007; Winn et al. 2007; Wolf et al. 2007). There is also a suggestion that the mass-period distribution for the injected planets (Nagasawa, Ida & Bessho 2008) is consistent with that observed for hot Jupiters (Marchi et al. 2009). However, a fractional loss of envelope during their periastron passage may lead to the ejection of gas giants on parabolic orbits (Guillochon, Ramirez-Ruiz & Lin 2011; Liu et al. 2013). Energy dissipation within the planets' envelope during the orbital circularization may also lead to substantial envelope inflation, mass loss, or total disruption (Gu, Lin & Bodenheimer 2003).

Around stars with pre-existing short-period gas giants (which may have migrated to the stellar proximity through disk-planet tidal interaction), a fresh injection of both gas giants and embryos raises the possibility of highly energetic merger and collision events. In the following sections, we present models based on the simulations of such events.

### 3 SPH AND GRID-BASED SIMULATIONS OF GIANT IMPACT AND MERGER OF GAS GIANTS

#### 3.1 Collisional Modelling Methods

In paper I, we considered only head-on parabolic collisions between embryos and gas giants. For long-period gas giants and for protoplanets near their ice-line natal site, their local Keplerian velocity ( $v_{\text{kep}} \sim 10 \text{ km s}^{-1}$ ) is generally smaller than their surface escape speed  $v_{\text{esc}} = (2GM_p/R_p)^{1/2}$ , so that their collisions are unlikely to be much more energetic than parabolic impacts. For hot Jupiters, however, the relative speed between (some parabolic) projectiles and target planets may exceed the local  $v_{\text{kep}}$  which is  $\geq 200 \text{ km s}^{-1}$ . In anticipation on these possibilities, we expand the range of impact speed in the simulated models presented here.

We model head-on and oblique collisions between planets using two complementary methods, smoothed particle hydrodynam-

ics (SPH) and an Eulerian grid-based code FLASH. Our SPH code is a descendant of the one used in Benz, Slattery & Cameron (1986) and includes self-gravity but neglects internal strength. We use an ideal gas equation of state for the gaseous envelope and the Tillotson equation of state for iron and basalt for condensed materials. The Tillotson equation of state relates pressure, density and internal energy of condensed materials and models them through three regimes. At low pressure this EOS captures the linear-shock particle relations and at high pressure the EOS extrapolates to the Thomas-Fermi limit. The Tillotson EOS also treats condensed material at low density as either a high energy gas or low energy and pressure fluid. Tillotson EOS parameters for particular materials (e.g., basalt, iron) are tuned to match results of laboratory experiments and theoretical limits (see Appendix A1 of Melosh 1989, for a brief discussion).

In addition, we use the Eulerian hydrodynamics code FLASH to construct several models with similar parameter used in SPH simulations. FLASH is a parallel, multidimensional hydrodynamics code based on block-structured adaptive mesh refinement (AMR). The center of the computational domain is fixed to the center of mass of the system and is  $4 \times 10^{13}$  cm on a side. We have made a careful choice of the refinement criteria, making our smallest cells only  $3.818 \times 10^7$  cm in width, which is less than 7 parts in 1000 of the planet's radius. Combing the vast simulation domain with high resolution at the center, we are able to keep track of the envelope expansion after the impact and resolve the planet's dense core simultaneously. Poisson equation is solved using a multipole expansion of the fluid with a maximum level at 40. Apart from from hydrodynamics and gravity, the two codes also differ in the equation of state (EOS). In FLASH simulations, we model the internal structure of the gas giant planet with composite polytropes with polytropic indices  $n_1 = 0.5$  and  $n_2 = 1$ , which can characterize the distinct chemical composition of the core and envelope of a gas giant planet (Liu et al. 2013). The embryo impactors are modeled with an  $n = 0.01$  polytrope with a central density  $\rho_c = 10 \text{ g cm}^{-3}$ . In this treatment, the polytropic constant  $K$  is a free parameter, and the polytropic model can be determined by given values of  $n$ ,  $M$  and  $R$  (Kippenhahn, Weigert & Weiss 2013). Here the choice of polytropic index  $n = 0.01$  over a more common value  $n \approx 1/3$  is made to give extra weight to the incompressible nature of the impactor. The polytropic index  $n$  of the impactor has little effect on the post-impact thermal evolution of the target in the sense that the kinetic energy of the impactor dominates its internal energy and the target has a much larger heat capacity than that of the impactor.

Our use of an ideal gas or polytrope EOS for the gaseous envelope simplifies the computation at the expense of omitting the processing of energy into internal degrees of freedom. Shock heating of the envelope resulting in dissociation and ionization of gas may act as a sink to mechanical impact energy and affect the final outcome of a collision (Zel'dovich & Raizer 1967). As a result, our use of simplified equations of state for the gaseous envelope may increase the fraction of energy retained in mechanical kinetic energy and the amount of material escaping a collision. Future work may address the significance of this issue with a more sophisticated equation of state and assess how of how this effect alters collisional processing of giant planets. However, our SPH and FLASH collisions models serve to illustrate the basic outcome morphologies and their implications for the collisional evolution of hot Jupiters.

This section is organized as follows. We first lay out our model of giant impact and merger. We then show that both codes produce

consistent results, although some discrepancies are found. Finally, we will discuss the causes for these discrepancies and use our results to predict observational signatures.

### 3.2 Range of impact speeds

In the limit that the orbits of two planets with  $\Delta a \ll a$  marginally cross within each other's Roche radius, their relative speed is

$$\Delta v \sim v_{\text{kep}}(a + \Delta a)(1 + \Delta a/a) - v_{\text{kep}}(a) \simeq v_{\text{kep}}(a)(\Delta a/2a). \quad (2)$$

Since gas giants' gravity also accelerates impactors, the impact speed associated with GIM's is generally larger than this value.

We first consider a system of planets which formed with nearly circular orbits. After the gas in the natal disks is depleted, their  $\Delta v$  grow and their orbits eventually cross each other on a time scale  $T_c$  (see Eq 1) with  $\Delta v \sim (GM_p/r_H)^{1/2} k_0 / \sqrt{12} \sim k_0/12^{1/3} (M_p/M_*)^{1/3} v_{\text{kep}}$ . For systems of gas giants, formed at a few AU's with  $k_0 \sim 6$ ,  $T_c$  is a few Gyr (ie comparable to the main sequence life span of the solar type stars). For impactors with much lower masses,  $\Delta a \sim 0.25a$  and  $\Delta v \sim 1 - 2 \text{ km/s}$ . Their values may increase by 25% for two gas giants with comparable masses.

Orbit crossing introduces finite collision probability rather than certain GIM's. The collision time scale depends on the differential orbital speed  $\Delta v$  at which impactors enter into the gas giants'  $r_H$ . For initial  $k_0 > 1$ ,  $\Delta v \sim (GM_p/r_H)^{1/2} \sim 3^{1/6} (M_p/M_*)^{1/3} v_{\text{kep}}$  and most encounters do not necessarily lead to physical collisions. Nevertheless, since  $\Delta v$  is much smaller than  $v_{\text{esc}}$ , planet's mutual gravitational attraction would accelerate them to attain impact speeds for parabolic encounters *i.e.*  $v_{\text{imp}} \simeq v_{\text{esc}}$ .

Numerical experiments (Zhou, Lin & Sun 2007) indicate that dynamical instability can be suppressed by eccentricity damping. In the proximity of their host stars, the eccentricity damping time scale due to planets' internal tidal dissipation (Goldreich & Soter 1966) is

$$\tau_e = \frac{4Q'_p}{63n_p} \left( \frac{M_p}{M_*} \right) \left( \frac{a}{R_p} \right)^5. \quad (3)$$

The planets' quality factor  $Q'_p \sim 10^6$  and  $\tau_e \sim 0.1 \text{ Gyr}$  are inferred for most transiting hot Jupiters from their observed eccentricity-mean motion ( $e - n_p$ ) distribution (Sasselov 2003; Ogilvie & Lin 2004). Most close-in super-Earths have smaller  $Q'_p$  and  $n_p$ , and comparable  $\tau_e$ . From equations 1 and 3, we estimate  $T_c \sim \tau_e$  with  $\Delta a \sim 0.3 - 0.4a$  for  $k_0 \sim 7$  for these planets. Their corresponding  $\Delta v$  is comparable to their  $v_{\text{esc}}$  such that the speed ( $v_{\text{imp}}$ ) of their giant impacts may range from a fraction to several  $v_{\text{esc}}$ . For our numerical models, we consider this entire range of possibilities.

### 3.3 Impact Orientation and Dynamics

We describe collision dynamics using  $v_{\text{imp}}$  and impact angle ( $\xi$ ). The magnitude of  $v_{\text{imp}}$  is a function of both the relative velocity at infinity ( $v_{\infty}$ ) and the two-body escape velocity ( $v_{\text{esc},2}$ ) with  $v_{\text{imp}}^2 = v_{\text{esc},2}^2 + v_{\infty}^2$ . For an encounter involving a target and impactor with masses ( $M_T, M_I$ ) and radii ( $R_T, R_I$ ) respectively, the two-body escape velocity is

$$v_{\text{esc},2}^2 = \frac{2G(M_I + M_T)}{(R_I + R_T)}. \quad (4)$$

In the limit  $M_I \ll M_T$  and  $R_I \ll R_T$ ,  $v_{\text{esc},2} \sim v_{\text{esc}}$ .

We have performed simulations of a range of impact speeds

with  $v_{\text{imp}}/v_{\text{esc},2} = 1, 1.4, 3,$  and  $5$ , which is consistent with the probable range of encounter velocities produced by multiple scattering events.

We use an impact angle ( $\xi$ ) defined as the angle between the relative position and velocity vectors when the surfaces of the two bodies are in contact (i.e.  $\xi = 0^\circ$  for a head-on collision and  $\xi = 90^\circ$  for a grazing, tangential encounter). Assuming an isotropic flux of impactors, the probability of a collision with  $\xi$  in the range  $\xi \rightarrow \xi + d\xi$  (Shoemaker 1962) is

$$dP = 2 \sin \xi \cos \xi d\xi. \quad (5)$$

The angle  $\xi = 45^\circ$  is the median value and the impact angles  $\xi = 30^\circ, 45^\circ, 60^\circ,$  and  $90^\circ$  divide the impact angle distribution into quartiles. We have performed simulations of both head-on  $\xi = 0^\circ$  collisions as well as more oblique collisions with impact angles of  $\xi = 21^\circ, 30^\circ, 45^\circ,$  and  $60^\circ$ . SPH simulations were run for about 24-hours of model time before analyzing the result. The simulations are first analyzed to determine the particles that are contiguous with the initial gas giant's core. Following that we determine which particles are gravitationally bound in a two-body sense. For FLASH simulations, we stop the simulations at about  $2 \times 10^5$  s. The determination of contiguous and bound material is more challenging in a grid code, and we describe our approach to measure these quantities in Section 3.7. Model parameters of SPH and FLASH simulations and their results are summarized in Tables 1, 2, and 3.

### 3.4 Collisions between a $25-M_\oplus$ embryo and a Saturn-mass gas giant

We simulate both head-on and oblique collisions between a Saturn-like  $100-M_\oplus$  gas giant planet and a  $25-M_\oplus$  embryo. SPH model parameters and results of this series of simulations are summarized in Table 1. These results are the generalization of the head-on parabolic collision in Paper I. In addition, four FLASH simulations with similar parameters are performed for comparison. Part of the analysis and visualization of the FLASH results in this work relies on the YT Python package (Turk et al. 2011).

The SPH simulations show that head-on collisions (with  $v_{\text{imp}} = 1 - 3v_{\text{esc},2}$ ) lead to the capture of the impactor by the gas giant and the coalescence of the impactor with the core. In addition, the envelope re-establishes a spherical symmetry within a dynamical time scale. These results justify the 1-D prescription and core-impactor coalescence assumption used in our LHD scheme (see Paper I). For sufficiently high velocity encounters, the energy dissipation near the core leads to a thermal expansion of the envelope. In model SA3a with  $v_{\text{imp}} = 3v_{\text{esc},2}$ , the impactor's kinetic energy is comparable to the gas giant's gravitational binding energy and a significant fraction of the envelope is lost. The requirement

$$v_{\text{imp}} > v_{\text{cri}} = (2(M_T + M_I)/M_I)^{1/2} v_{\text{esc},2} \quad (6)$$

corresponds to the condition for total disruption of isolated gas giants. Note that in model SA4a with  $v_{\text{imp}} = 5v_{\text{esc},2}$ , the impact energy is so large that both the envelope and core totally disintegrated. Anderson & Adams (2012) predicted a penetration velocity for head-on collisions four orders of magnitude greater than the escape velocity. Such energetic collisions likely lead to destruction of the gas giant other than penetration according to our results.

Despite the general agreement between Equation 6 and the SPH results in Table 1, some of the results obtained through these

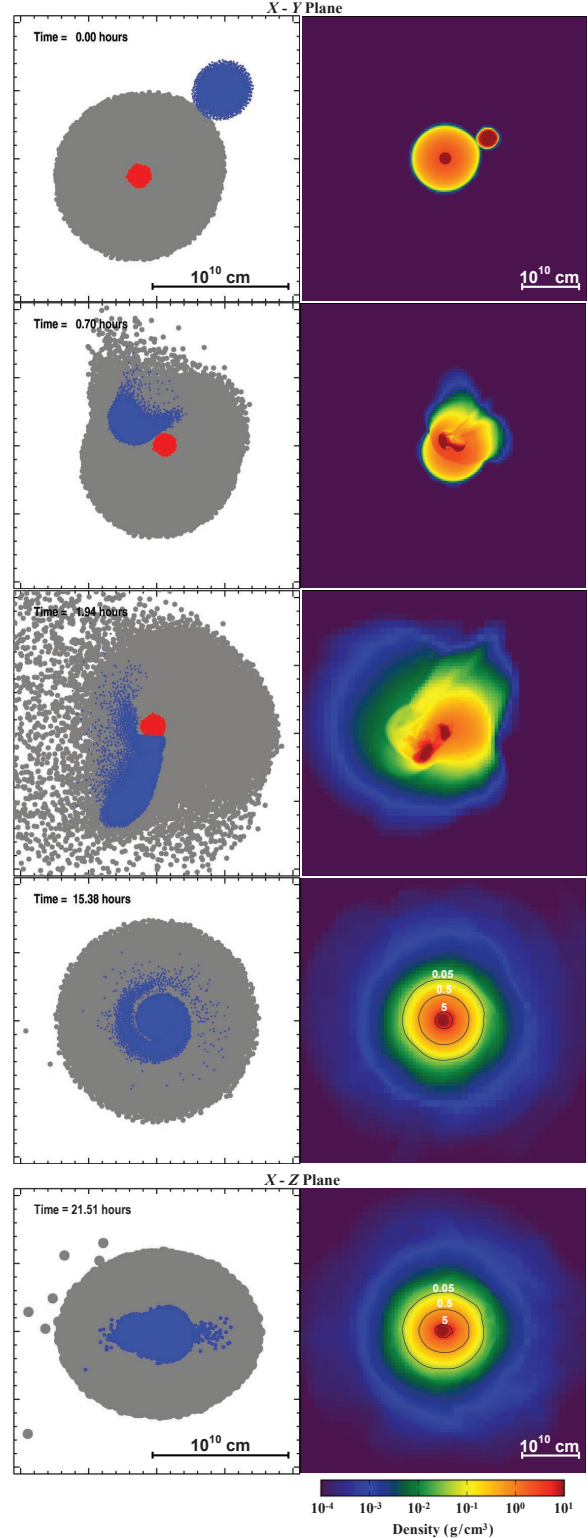


**Figure 2.** Comparison of collision between a Saturn-like gas giant and a  $25-M_\oplus$  impactor. In the SPH model SA1c (left column), gas particles are shown as grey, and core particles (iron) are over plotted in red. The basalt impactor is over plotted in blue. In the FLASH model FA1c (right column), color denotes gas density, and the black lines in the last two frames are the contour lines at  $\rho = 5, 0.5$  and  $0.05 \text{ g cm}^{-3}$ , respectively. The upper four rows are slices through the orbital plane (the initial motion is along the X-axis) and the lower one is the slices through the plane which perpendicular to the orbital plane.

Model	$\xi$	$v_{\text{imp}}/v_{\text{esc},2}$	$M_{\text{bm}}$	$M_{\text{bm},c}$	$R_{\text{bm}}/R_{\text{T}}$	$M_{\text{cc}}$	$M_{\text{cc},c}$	$R_{\text{cc}}/R_{\text{T}}$	$J_{\text{cc}}/J_{*}$
SPH									
SA1a	0	1.0	125.0	35.0	1.08	107.9	35.0	0.95	0.001
SA1b	21	1.0	124.7	35.0	1.08	104.2	35.0	0.92	0.168
SA1c	30	1.0	124.7	35.0	1.08	101.9	35.0	0.90	0.219
SA1d	45	1.0	124.7	35.0	1.09	96.3	34.3	0.88	0.261
SA1e	60	1.0	125.1	35.0	1.03	90.5	10.4	0.94	0.069
SA2a	0	1.4	123.1	35.0	1.09	102.8	35.0	0.93	0.001
SA2b	21	1.4	122.9	35.0	1.09	97.2	35.0	0.89	0.210
SA2c	30	1.4	123.0	35.0	1.10	93.8	34.6	0.87	0.263
SA2d	45	1.4	99.1	10.8	1.02	88.5	10.4	0.93	0.065
SA2e	60	1.4	99.9	10.2	1.01	93.2	10.1	0.95	0.034
SA3a	0	3.0	87.9	35.0	0.84	80.3	34.7	0.78	0.001
SA3b	21	3.0	85.5	11.5	1.00	67.6	11.1	0.84	0.070
SA3c	30	3.0	92.6	10.5	1.03	74.6	10.3	0.88	0.064
SA3d	45	3.0	98.2	10.2	1.03	85.2	10.0	0.92	0.048
SA3e	60	3.0	99.8	10.0	1.01	92.8	10.0	0.95	0.021
SA4a	0	5.0	0.4	0.3	0.11	0.1	0.1	0.07	0.229
SA4b	21	5.0	69.5	10.3	0.90	58.0	10.1	0.79	0.059
SA4c	30	5.0	85.5	10.2	1.01	67.8	10.1	0.85	0.051
SA4d	45	5.0	96.4	10.1	1.04	80.7	10.0	0.91	0.048
SA4e	60	5.0	99.5	10.0	1.02	89.9	10.0	0.94	0.026
FLASH									
FA1c	30	1.0	121.1	34.4	12.67	117.1	34.4	3.34	0.066
FA2a	0	1.4	115.3	34.3	7.09	108.6	34.3	2.58	$5 \times 10^{-5}$
FA3a	0	3.0	8.5	5.4	6.49	8.5	5.4	6.49	$10^{-4}$
FA3c	30	3.0	83.2	10.0	8.44	76.9	10.0	2.34	0.003

**Table 1.** Collisions between a  $100M_{\oplus}$  gas giant and a  $25M_{\oplus}$  embryo. The gas giant planet was modelled with 30,000 particles. The number of particles in the impactors were adjusted to maintain equal particle mass with the gas giant target planet. At the end of the simulation the mass and radius of the material contiguous with the core of the initial gas giant planet are listed as  $M_{\text{cc}}$  and  $R_{\text{cc}}$ . The total mass gravitationally bound particles and their equivalent radius are labelled as  $M_{\text{bm}}$  and  $R_{\text{bm}}$ . The difference between these quantities reflects material in a protosatellite disk or distant material that has yet to fall back to the planet. All masses are in  $M_{\oplus}$ . Planets' initial radius and the asymptotic radius when a quasi hydrostatic equilibrium is re-established after the GIM's are represented by  $R_{\text{T}}$  and  $R_{\text{cc}}$  respectively, where  $R_{\text{T}} = 5.99 \times 10^9$  cm. In the asymptotic state, we also compare mergers' angular momentum  $J_{\text{cc}}$  and compare it with that associated with rotational break up.

SPH simulations are possibly due to numerical artefacts. For example, the ratio of the final to initial planetary radius ( $R_{\text{T}}/R_{\text{i}}$ ) remains close to unity for head-on collisions with  $v_{\text{imp}} < 3v_{\text{esc},2}$ . This negligible change in the gas giant's envelope is partially due to the artificial lower density limit we have adopted for the SPH scheme (*i.e.*  $\rho_{\text{l}} = 0.5 \text{ g cm}^{-3}$ ). This restriction prevents the dispersal of representative fluid elements into tenuous medium. This technical limitation is clearly shown by the sharp density fall off at the gas giant's new radius. This prescription may also over suppress the loss of gas in the giant's original envelope as a consequence of high-speed collisions (see §4.2). The actual critical impact speed required for substantial collision-induced mass loss may be substantially reduced in the proximity of the host star.

Without such restriction of lower density limit, the FLASH code is ideal to study the expansion of the gas giant's envelope after the impact. Consequently, the determination of different boundaries in FLASH simulations is also challenging (see Section 3.7). In run FA2a we find much larger  $R_{\text{cc}}$  and  $R_{\text{bm}}$  than those in run SA2a, while the enclosed masses  $M_{\text{cc}}$  and  $M_{\text{bm}}$  are slightly less than that in SPH. Besides, in model FA3a with  $v_{\text{imp}}$  3 times the  $v_{\text{esc},2}$ , the impactor is able to disintegrate the gas giant, while under the same circumstances, SPH model SA3c shows that most of the original mass of the gas giant is retained after the impact.

We also illustrate the results of oblique collisions, first with the parabolic impact speed ( $v_{\text{imp}} = v_{\text{esc},2}$ ). In this low-energy limit, the impactor is always consumed by the gas giants. Over most range of  $\xi$ , say  $\xi < 60^\circ$ , the impactor is able to penetrate through the gas giant's envelope, to merge with its core in a few dynamical timescales. This tendency is well illustrated in Figure 2, which shows the SPH particles distribution of model SA1c and density slice of model FA1c in the orbital plane (designated to be the  $X$ - $Y$  plane with the initial motion along the  $X$ -axis) for four different epochs. We also plot the particles distribution and density slice in the the  $X$ - $Z$  plane (where  $Z$ -axis is the axis normal to the orbital plane).

We notice that the asymptotic core radius increases with  $\xi$  (in comparison with the Figure 1 in Paper I). In the limit of collisions with relatively large  $\xi$ , the impactor is disintegrated in the envelope well outside the iron core. If the debris of the impactor remains separated from gaseous material in the envelope of the gas giant, double-diffusive convection may kick in, and the compositional transport rate could be either very small or relatively large (Rosenblum et al. 2011). In other word, whether the debris will dissolve in the envelope or eventually sediment into the core is not clear yet. Either way, the time scale to re-establish a hydrostatic equilibrium is considerably longer than the dynamical timescale.

This fractionation process provides a protracted source of energy to sustain a relatively large planet radius  $R_p$  after the impact. The FLASH run FA1c shows similar consequences of the impact except that the final structure is much puffier and mass loss is slightly higher, as we have noticed in the head-on cases.

The bottom panel of Figure 2 is an edge-on view of the planet after the impact, which indicates a rotational flattening structure in the gas giant which has been struck by an embryo at a modest grazing angles  $30^\circ$ . The capture of an embryo modifies the spin angular momentum of the gas giant by an amount  $\Delta J \simeq M_1 R_T v_{\text{imp}} \sin \xi$ . If the gas giant does not have any initial spin, the ratio of its final angular momentum  $J_f = \Delta J$  and that corresponds to a rotational breakup ( $J_c \sim (M_T + M_1) R_p v_{\text{esc},2}$ ) would be

$$\frac{J_f}{J_c} \simeq \frac{M_1}{(M_T + M_1)} \left( \frac{v_{\text{imp}}}{v_{\text{esc},2}} \right) \sin \xi, \quad (7)$$

where we have assumed  $R_p \simeq R_T$ . This estimate is in good agreement with those listed in Table 1. In general, the angular momentum deposited by the impactor is not uniformly distributed throughout the planet. And one may notice that the ellipticity of isodensity contours of the edge-on view of run FA1c slightly decreases from inside to outside. Furthermore, different types of giant impact produce distinguished signatures of oblateness (see Section 3.8). Here we simply assume this spin angular momentum is smoothly distributed throughout the gas giant's envelope as a first-order approximation, it would speed with a frequency  $\Omega_f \sim (J_f/J_c)(v_{\text{esc},2}/\alpha_p R_p)$ , where  $\alpha_p$  is the coefficient for the moment of inertia. For isolated long-period gas giants, a parabolic GIM by a super-Earth impactor with  $M_1 < 0.1 M_T$  would not lead to rotational breakup. But, in the limit that  $J_f = \Delta J$ ,

$$\frac{\Omega_f}{n_p} \simeq \frac{M_1}{(M_T + M_1)} \left( \frac{v_{\text{imp}}}{v_{\text{esc},2}} \right) \left( \frac{3R_H}{R_p} \right)^{3/2} \sin \xi, \quad (8)$$

where  $R_H$  is the Hill radius of the giant planet. For hot Jupiters,  $\Omega_f$  can be significantly larger than the rotational frequency associated with the spin-orbit synchronization ( $\sim n_p$ ). Thus, stochastic parabolic collisions by super-Earths can offset synchronous spin generally associated with star-planet tidal interaction.

For high-energy oblique collisions, impactor's capture probability decreases with both  $\xi$  and  $v_{\text{imp}}$ . During impactor's first passage, the total amount of kinetic energy lost due to hydrodynamic drag alone is

$$\Delta E_k = M_1(v_{\text{imp}}^2 - v_{\text{final}}^2)/2 \simeq M_1 v_{\text{imp}} \Delta v / 2, \quad (9)$$

where  $v_{\text{final}}$  is the impactor's velocity after it passes through the target and  $\Delta v = v_{\text{imp}} - v_{\text{final}}$  is the change of the impactor's velocity. Because momentum is conserved, we have  $M_1 \Delta v \simeq M_{\text{enc}} v_{\text{imp}}$  and

$$M_{\text{enc}}(\xi) \simeq \int_L \rho A dl \simeq \frac{2AR_p \cos \xi}{1 - \sin \xi} \int_{\sin \xi}^1 \rho(x) dx \quad (10)$$

is the "air mass" encountered by the impactor in the gas giant's envelope,  $L$  is impactor's trajectory inside the gas giant and the gas density  $\rho$  is a function of distance from the gas giant's center  $R$  or equivalent a function of  $x \equiv R/R_p$ . For modest impacts, impactor's effective cross section  $A$  is comparable to its physical radius  $R_1$ . In the above expression  $M_{\text{enc}}$  is a rapidly decreasing function of the impact angle  $\xi$ .

We now determine the capture cross section of embryos by the gas giant. An impactor is unlikely to be captured in the limit that  $\Delta E_k < M_1(v_{\text{imp}}^2 - v_{\text{esc},2}^2)/2$  or equivalently

$$M_{\text{enc}} < M_1 \left( 1 - (v_{\text{esc},2}/v_{\text{imp}})^2 \right) / 2. \quad (11)$$

The air mass required for capturing an intruding embryo with low impact speed is a small fraction of  $M_1$ . Provided the impact parameter is smaller than the gas giant's radius  $R_p$  (*i.e.*  $\cos \xi$  is non-negligible), most parabolic encounters leads to coalescence. But, the required air mass  $M_{\text{enc}} \sim M_1/2$  for high impact speed collisions. Capture of relatively massive embryos would be possible only for relatively small  $\xi$ , *i.e.* nearly head-on collisions. Similar arguments have been used to estimate the fraction of material lifted into the proto-lunar disk via giant impact (Canup 2008) and the mechanical energy dissipated in collisions between stars (Freitag & Benz 2005) and planets (Leinhardt & Stewart 2012).

The capture condition in equation 11 is in good agreement with the simulation results in Table 1, *i.e.* collisions with a high impact speeds and angles generally do not lead to capture whereas embryos which impinges onto gas giants with relative low impact speeds and angle generally merge with them. These general outcome morphologies have also been observed in collisions between stars and planets (Agnor & Asphaug 2004; Freitag & Benz 2005; Asphaug, Agnor & Williams 2006; Marcus et al. 2009; Leinhardt & Stewart 2012) and appear a scale-invariant feature of gravity-dominated collisions.

With a high relative speed, the impactor also disintegrates when it encounters an air mass comparable to its own. Because when  $M_{\text{enc}} \sim M_1$ , the change of the impactor's total energy is comparable to its gravitational binding energy. Thus, in the limit of high velocity encounters, captured embryos rapidly disintegrate whereas the flyby embryos essentially retain their initial mass.

Finally, we point out that among all the simulations in which the planet is not destroyed, the mass loss is preferentially comes from the envelope other than the core. In fact, there is only very tiny mass loss contributed by the core. This result indicates that giant impacts may lead to the enhanced metallicity in the envelopes of gas giants.

### 3.5 Collisions between a $10-M_\oplus$ embryo and a Saturn-mass gas giant

Here, we consider a series of models which simulate the collision between a Saturn-like giant planet and a  $10-M_\oplus$  embryo. Model parameters and results of this series of simulations are summarized in Table 2. We emphasize here that relatively low-mass embryos disintegrate in the envelope before reaching the core.

The results in Table 2 are qualitatively similar to those in Table 1, *i.e.* all head-on and all low-speed collisions lead to the capture of this relatively low-mass embryo and oblique high-velocity embryos pass through and escape from the gas giant's envelope.

In contrast to the  $25-M_\oplus$  models, this lower mass ( $10-M_\oplus$ ) impactor's kinetic energy is inadequate to disrupt gas giant's envelope in all SPH simulations. Note that in FLASH simulations, only the high-speed head-on collision (FB4a) can disrupt the gas giant. In some high-speed impacts (such as model SB4b), sufficient energy is deposited to the envelope to induces fractional mass loss, even though the impactor is not captured during the encounter. Nevertheless, it can carry sufficient amount of energy, especially through high-velocity encounters, to perturb the structure of the gas giant (albeit SPH scheme may not be able to resolve these changes), Cap-

Model	$\xi$	$v_{\text{imp}}/v_{\text{esc},2}$	$M_{\text{bm}}$	$M_{\text{bm},c}$	$R_{\text{bm}}/R_{\text{T}}$	$M_{\text{cc}}$	$M_{\text{cc},c}$	$R_{\text{cc}}/R_{\text{T}}$	$J_{\text{cc}}/J_{*}$
SPH									
SB1a	0	1.0	110.1	20.0	1.06	96.9	20.0	0.95	0.001
SB1b	21	1.0	110.1	20.0	1.05	97.0	20.0	0.95	0.097
SB1c	30	1.0	110.0	20.0	1.05	96.2	20.0	0.94	0.132
SB1d	45	1.0	109.7	20.0	1.05	94.3	18.7	0.93	0.155
SB1e	60	1.0	109.8	20.0	1.03	100.2	19.6	0.96	0.246
SB2									
SB2a	0	1.4	110.1	20.0	1.07	92.8	20.0	0.94	0.001
SB2b	21	1.4	109.5	20.0	1.07	92.2	20.0	0.93	0.122
SB2c	30	1.4	109.1	20.0	1.06	91.0	19.7	0.92	0.163
SB2d	45	1.4	100.3	11.4	1.02	91.2	11.0	0.94	0.056
SB2e	60	1.4	100.2	10.4	1.00	94.0	10.1	0.95	0.023
SB3									
SB3a	0	3.0	100.5	20.0	1.06	79.4	20.0	0.89	0.002
SB3b	21	3.0	93.3	11.6	1.04	73.7	11.1	0.88	0.070
SB3c	30	3.0	95.6	10.6	1.04	79.8	10.3	0.91	0.061
SB3d	45	3.0	98.7	10.1	1.02	87.3	10.0	0.93	0.038
SB3e	60	3.0	99.9	10.1	1.01	93.2	10.0	0.95	0.017
SB4									
SB4a	0	5.0	64.9	19.7	0.78	55.7	19.3	0.69	0.003
SB4b	21	5.0	82.0	10.5	0.99	64.5	10.2	0.83	0.049
SB4c	30	5.0	90.8	10.2	1.03	72.4	10.1	0.88	0.049
SB4d	45	5.0	97.5	10.0	1.03	83.6	10.0	0.92	0.042
SB4e	60	5.0	99.6	10.0	1.01	91.4	10.0	0.95	0.022
FLASH									
FB3a	0	3.0	65.9	14.9	4.52	65.9	14.9	4.52	$10^{-4}$
FB3c	30	3.0	88.9	10.1	8.42	80.5	10.0	1.55	0.004
FB4a	0	5.0	-	-	-	-	-	-	-

**Table 2.** Collisions between a Saturn-mass gas giant and a  $10-M_{\oplus}$  embryo. The symbols have identical meanings of those in Table 1.

tered embryos can also deposit a significant amount of spin angular momentum to the gas giant.

Model parameters for the low-mass embryo to be marginally captured are in good agreement with equation (11). The captured models indicate that spin angular momentum deposited into the envelope is greater than that needed for some hot Jupiters to uniformly rotate with an angular frequency which synchronizes with their orbital frequency. In contrast, gas giant's mass and angular momentum are not significantly affected by fly-by encounters. But, in some models (such as SB2d and SB3b) a fraction of the impactor's mass can be stripped from it during its passage through (rather than capture by) the gas giant's envelope. As a result, the final core mass slightly increases. Model SB2c indicates that during oblique collisions with modest energy, this modest size embryo is mostly disrupted, which is similar to model SA1c except that most of the mass is deposited in the gas giant's envelope, slightly outside the iron core. The kinetic energy of the impactor is also deposited in the envelope rather than near the core. Eventual sedimentation of impactor's fragments releases additional energy on a much longer time scale (see §4). In contrast, model SB3c shows that highly energetic embryos may not be retained by the envelope of the gas giant that they have oblique collisions with. In FLASH simulation FB3c, the impactor penetrate through the gas giant's envelope as well, and causing over 10% of gas giant's mass is unbound and its outer envelope becomes very extensive but its inner region remains unchanged (Figure 3). The amount of angular momentum deposition is also correspondingly less than the total-coalescence models with the same impact parameter.

These figures also indicate that although spherical symmetry

is temporarily destroyed during the impact, it is quickly restored both in the envelope and the core after 1-2 dynamical time scales. Despite the injection of spin angular momentum to the gas giant's envelope, the asymptotic distribution of the debris is approximately spherically symmetric.

### 3.6 Merger between two Saturn-mass gas giants

In this subsection, we present simulations of collisions between two identical gas giants. Similar to the previous section, we adopt an initial model with a  $90-M_{\oplus}$  envelope around a  $10-M_{\oplus}$  core. We also explore a similar series of initial conditions which are listed in Table 3.

These models again indicate that parabolic encounters lead to the total coalescence of gas giants without any loss of heavy elements in the cores and gas in the envelopes. In order to compare with results of the head-on parabolic merger, we present the results of model SC1b and FC1b in Figure 4.

These results indicate that the cores preserve their integrity until they are in contact with each other. During the collision, the iron cores of both gas giants are thoroughly mixed each other. These simulations also show that the internal structure of the merger product rapidly becomes symmetric about the Z-axis. Even with this small impact angle, the merger product acquires a substantial amount of spin angular momentum, primarily due to the relatively large mass of the impactor.

In the SPH simulation, the asymptotic major axis (in the orbital planet) of the merger product is larger than the gas giant's initial radius  $R_p$ . The polar radius  $R_{p0}$  (i.e.  $R_p$  in the X-Z plane)

Model	$\xi$	$v_{\text{imp}}/v_{\text{esc},2}$	$M_{\text{bm}}$	$M_{\text{bm},c}$	$R_{\text{bm}}/R_{\text{T}}$	$M_{\text{cc}}$	$M_{\text{cc},c}$	$R_{\text{cc}}/R_{\text{T}}$	$J_{\text{cc}}/J_{*}$
SPH									
SC1a	0	1.0	199.6	20.0	1.25	178.0	20.0	1.13	0.000
SC1b	21	1.0	200.1	20.0	1.27	159.8	20.0	1.05	0.258
SC1c	30	1.0	200.3	20.0	1.32	144.9	20.0	1.02	0.299
SC1d	45	1.0	200.3	20.0	1.27	151.5	20.0	1.02	0.744
SC1e	60	1.0	200.3	20.0	1.29	87.6	10.0	0.92	0.118
SC2a	0	1.4	197.8	20.0	1.27	168.0	20.0	1.11	0.001
SC2b	21	1.4	199.3	20.0	1.33	138.7	20.0	1.00	0.276
SC2c	30	1.4	199.9	20.0	1.34	77.3	10.0	0.88	0.150
SC2d	45	1.4	100.0	10.0	1.04	85.4	10.0	0.92	0.087
SC2e	60	1.4	100.0	10.0	1.02	91.0	10.0	0.94	0.063
SC3a	0	3.0	112.1	20.0	0.89	98.1	19.5	0.82	0.001
SC3b	21	3.0	69.2	10.0	0.84	62.1	10.0	0.77	0.155
SC3c	30	3.0	87.4	10.0	1.01	70.7	10.0	0.86	0.069
SC3d	45	3.0	97.5	10.0	1.04	81.0	10.0	0.91	0.061
SC3e	60	3.0	99.6	10.0	1.01	91.3	10.0	0.95	0.034
SC4a	0	5.0	41.7	13.1	0.55	36.3	12.4	0.51	0.005
SC4b	21	5.0	48.0	10.0	0.62	44.0	10.0	0.57	0.126
SC4c	30	5.0	70.0	10.0	0.87	62.9	10.0	0.80	0.084
SC4d	45	5.0	93.6	10.0	1.04	74.9	10.0	0.88	0.055
SC4e	60	5.0	99.2	10.0	1.03	87.3	10.0	0.93	0.037
FLASH									
FC1b	21	1.0	196.3	20.0	9.76	188.1	20.0	3.43	0.181
FC2a	0	1.4	169.2	20.0	12.47	148.0	20.0	3.49	$2 \times 10^{-4}$

**Table 3.** Collisions between two  $100-M_{\oplus}$  gas giant planets. The symbols have identical meanings of those in Table 1.

remains unaltered from the initial  $R_p$ . But this difference between major and minor axes indicate that the enlargement of equatorial radius  $R_{\text{eq}}$  (i.e.  $R_p$  in the  $X$ - $Y$  plane) is mainly due to the rotational effects rather than thermal expansion. Indeed, the amount of energy dissipation during the collision is actually a modest fraction of the gas giant’s initial internal energy.

In the FLASH simulation, both  $R_{\text{po}}$  and  $R_{\text{eq}}$  of the merger product expand, but  $R_{\text{eq}}$  is also much larger than  $R_{\text{po}}$ . We will discuss the oblateness of FLASH simulations in Section 3.8.

For highly oblique collisions (models SC1d and SC1e), the spin angular momentum of the merger product is comparable to the break up speed. There is likely to be substantial tidal evolution toward spin synchronization. The continuous influx of internal energy can lead to substantial tidal heating and possibly loss of envelope mass (Gu, Lin & Bodenheimer 2003; Gu, Bodenheimer & Lin 2004).

For relatively high impact velocities ( $v_{\text{imp}}/v_{\text{esc},2} = 1.4$ ) and small-impact angle collisions ( $\xi < 30^\circ$ ), the condensed materials of the impactor and target effectively merge with little loss of the gaseous envelope. However, for more oblique collisions (models SC2d and SC2e), the energy dissipation during the impact is insufficient to bind the colliding gas giants. They continue their original course with a small amount of energy loss and no mass loss.

With a higher impact speed ( $v_{\text{imp}}/v_{\text{esc},2} = 3$ ), a head-on collision leads to the loss of most (more than half), but not all of initial envelope gas while the two cores merged (model SC3a). For collisions with modest impact angles ( $\xi = 21^\circ$ , model SC3b), merger of the cores is avoided while each gas giant loses a substantial (up to 1/3) fraction of its initial envelope. Given that half of collisions have non negligible  $\xi$ , these non-accretionary, envelope-

eroding collisions are as probable as core-merging collisions. These intermediate-mass (between Jupiter and the Earth) merger products may account for the unexpected presence of some planets in the domain of “planet desert” (Ida & Lin 2004; Howard et al. 2010; Ida, Lin & Nagasawa 2013).

For highly oblique encounters (with  $\xi \geq 30^\circ$ , models SC3c, SC3d and SC3e), gas giants retain their original envelope, albeit considerable angular momentum is deposited to the gas giant’s spin during gas giants’ brief passage through each other’s envelope.

Hyper-velocity head-on collisions (with  $v_{\text{imp}}/v_{\text{esc},2} = 5$ ) lead to the non-equal fragmentation of both core and envelope. Finally, after high-velocity oblique collisions, cores continue their original fly paths with a fraction of their initial envelopes. In contrast to the substantial (but not entire) losses of gas giants’ initial envelope, most of the core material is retained by the merger product. Thus, the metallicity of the merger product always increases from that of the original gas giant planets. Finally, these collisions deposit not only energy and heavy elements but also angular momentum to the spin of the colliding gas giants.

### 3.7 Comparison between SPH and FLASH results

Both SPH and grid codes have been widely used to perform hydrodynamic simulations. Because of their inherent differences, SPH and grid methods are complementary to study the same problem. For example Canup, Barr & Crawford (2013) compared these two methods in the context of the lunar-forming impacts, and they found a general agreement between the SPH and the grid code. In this work, we confirm that the SPH and the FLASH codes produce overall agreement on the critical impact speed for the envelope and

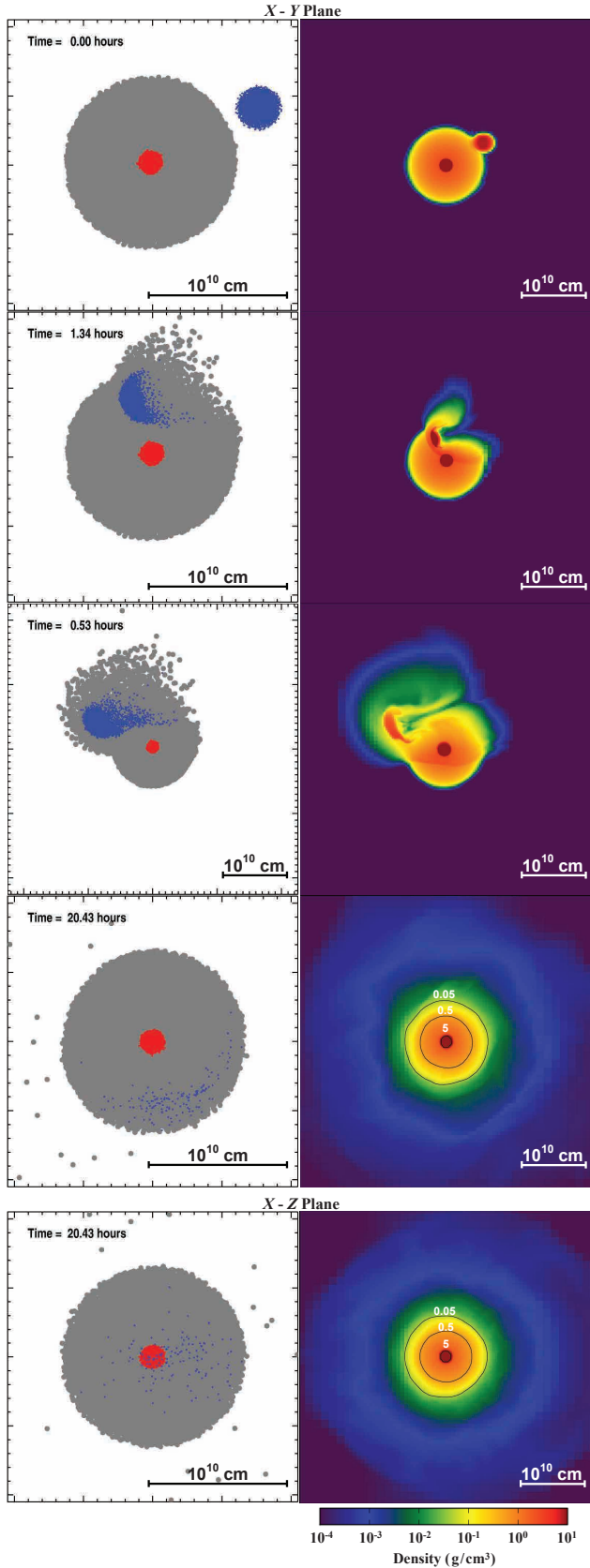


**Figure 3.** SPH run SB3c (left) and FLASH run FB3c (right) simulations of the collision between a Saturn-like gas giant and a  $10 M_{\odot}$  impactor. In the SPH simulation, gas particles are shown as grey, and core particles are over plotted in red. The basalt impactor is over plotted in blue.  
 © 0000 RAS, MNRAS 000, 000–000

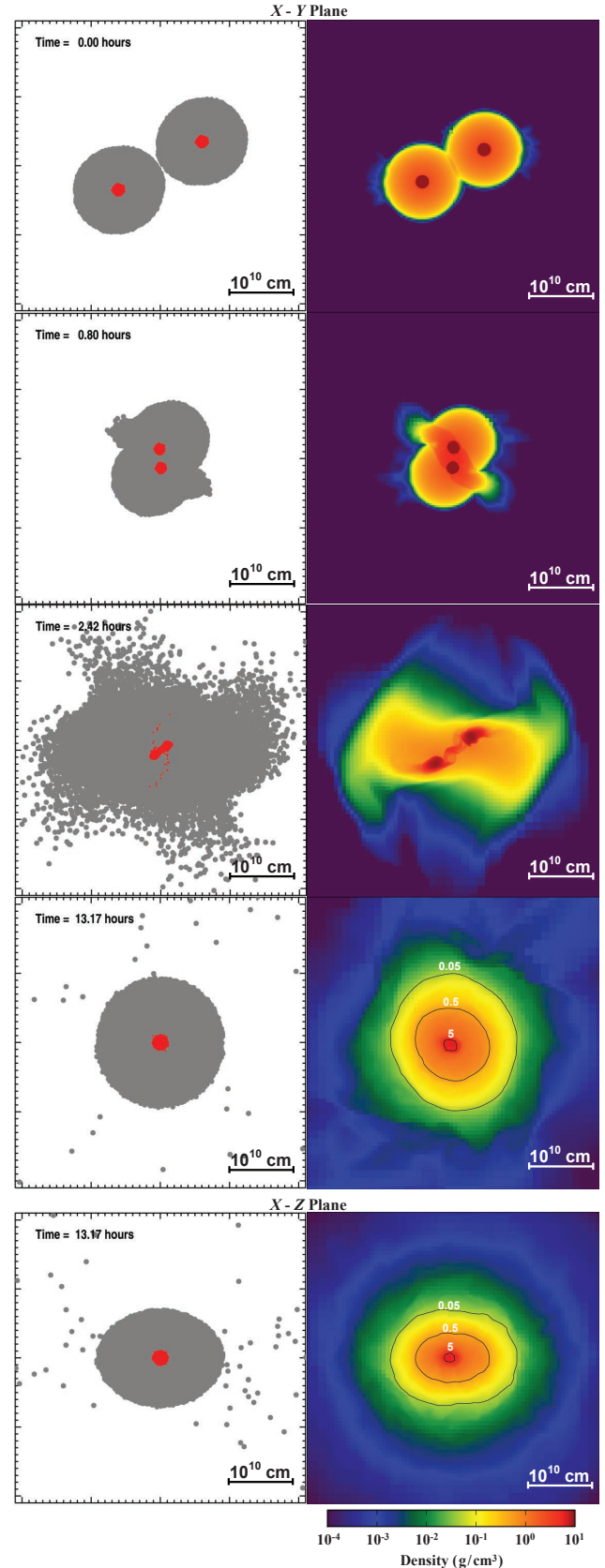


**Figure 4.** SPH run SC1b (left) and FLASH run FC1b (right) simulations of the merger between two Saturn-like gas giants. In the SPH simulation, gas particles are shown as grey, and core particles are over plotted in red.

core mass losses, even though they differ in the size of resultant collisions.

Apart from the hydrodynamics, gravity and EOS, the two codes also differ in the treatment of the ambient medium. The SPH simulations incorporate a density limit  $\rho_l = 0.5 \text{ g cm}^{-3}$  to prevent spreading of very low density gas (that is not well-resolved in an SPH model with equal particle mass). The density limit acts as an external pressure, and the expansion of the particle stops at the density limit and the particle then evolves due to gravity and whatever neighbors it is interacting with hydrodynamically.

It is known that AMR codes are very suitable to deal with surrounding structure around a dense object given that the minimum-grid and refinement criteria are made to capture the dense region (Tasker et al. 2008). In our grid scheme, we adopt a density  $\rho = 10^{-19} \text{ g cm}^{-3}$  for the ambient medium, so gas can diffuse into tenuous interplanetary space. As a result, all the FLASH simulations produce much puffier gas giants than those observed in the SPH runs.

However, to determine the corresponding contiguous and bound radii  $R_{cc}$  and  $R_{bm}$  in FLASH is less straightforward because the gas density gradually decreases all the way down to the ambient medium level at a fairly large distance (usually two orders of magnitude larger than the original size of the planet). Furthermore, simply prolong the simulation until the planet is fully relaxed is inefficient and may introduce other accumulative errors.

Here we use the mass flux  $\dot{M}$  to quantitatively analyze the structure of the planet. The  $\dot{M}$  at a given radius is the amount of mass that is flowing out through the sphere with that radius, e.g., a positive  $\dot{M}$  indicates an outflow (and vice versa). A post-impact sequence of the mass flux  $\dot{M}$  as a function of the radius taken from FC1b is plotted in the left panel of Figure 5. Ten successive snapshots of mass flux  $\dot{M}$  with a constant separation of 5000 s are presented in different colors. Even almost 2 days after the impact, the FLASH result shows that large-amplitude oscillations of mass flow are still prevailing throughout the whole planet, which suggests that the relaxation time scale is much longer than the dynamical timescale. On the outskirts of the planet where the density drops below  $10^{-2} \text{ g cm}^{-3}$  (see Figure 4), the amplitude of such oscillations gradually decreases. As the distance goes further, the amount of mass flux overturns representing the gas outflow due to the merger. The position of the peak increases with time whereas the value of the peak decrease, which suggests the inner part does not replenish the outflow.

We plotted the time-averaged mass flux of the ten snapshots in the thick black line in the right panel of Figure 5. We define the contiguous radius  $R_{cc}$  as the radius within which large-amplitude oscillations of  $\dot{M}$  occur but the averaged  $\dot{M}$  is much reduced, so the net mass flow is orders of magnitude smaller than the instantaneous value. The bound radius  $R_{bm}$  is defined as the separation between the bound mass and unbound mass. Material in the region surrounded by spheres with  $R_{cc}$  and  $R_{bm}$  is very tenuous and but still bound to the planet. It may form a protosatellite disk or be stripped off due to other perturbations such as tidal interactions.

The definitions of  $R_{cc}$  and  $R_{bm}$  are somewhat less stringent in the sense that these boundaries may evolve with time. Considering the planet will cool off due to thermal radiation, the contiguous radius  $R_{cc}$  is likely to become smaller. As the planet adjusts its internal structure to cooling, it becomes more similar to that produced by SPH simulations. On the other hand, the removal of the outflow may also lead to the expansion of  $R_{bm}$ . In the context of the

planetary system, the  $R_{bm}$  is comparable to its Hill radius. However, we notice that the net mass flow is negligible - in other words, the enclosed mass does not change despite the evolution the  $R_{cc}$  and  $R_{bm}$ . In this work, we measure the two radii at the time about 2 days after the impacts or mergers in all FLASH simulations.

### 3.8 Oblateness as an observable signature of GIM

Oblique impacts or mergers deposit angular momentum into the gas giant planet and alter its shape as well as its spin axis. To describe the shape of a planet, it is useful to define the oblateness as

$$f \equiv \frac{R_{eq} - R_{po}}{R_{eq}}, \quad (12)$$

where  $R_{eq}$  and  $R_{po}$  are the equatorial radius and the polar radius, respectively. In Figure 6, we plot the oblateness  $f$  of isodensity surfaces from the interior to the surface of the planet. Three FLASH simulations FA1c, FB3c and FC1b are investigated. The oblateness profile is obtained by measuring the  $R_{eq}$  and  $R_{po}$  of many isodensity surfaces. Each simulation represents a possible scenario in giant impacts or mergers.

In the simulation FB3c, a  $10-M_{\oplus}$  embryo penetrates the gas giant's envelope rapidly leaving the bulk structure of the gas giant mostly unchanged. The time for the impactor to exert a torque to spin up the gas giant is short. As a result, the embryo does not deposit much angular momentum into the gas giant, so the oblateness  $f$  remains close to 0 throughout.

In the other giant impact simulation FA1c, a  $25-M_{\oplus}$  embryo is disintegrated near the gas giant's core and deposit a large amount of angular momentum there. Therefore, the oblateness  $f$  keeps a relatively high level in the interior (say  $\rho > 1 \text{ g cm}^{-3}$ ) and drops quickly to a sub-Saturn level at larger radii. In another words, the gas giant gains much more angular momentum than that in the previous case, but its observable shape does not differ very much from a sphere as  $f$  is small in the surface layer.

Nevertheless, the simulation FC1b shows an opposite pattern of  $f$ , in which  $f$  is small in the interior and becomes prominent near the surface. That is because during the oblique merger of two equal mass gas giants, torque exerted on different parts varies a lot, which introduces differential rotation to the planet. As a result, the envelope spins faster than the core and  $f$  peaks near the surface and remains significant at the outer boundary.

Inspired by these dramatic differences, we propose that the oblateness may serve as a proxy for probing the impact history of gas giant planets given that the exchange of angular momentum between the planet and host star can be ignored. Giant impacts generally do not lead to large oblateness, while gas giant mergers do. An oblate transiting extrasolar planet would have a discernible effect on transit light curves (Hui & Seager 2002; Seager & Hui 2002; Barnes & Fortney 2003). Combing the oblateness information with other physical properties like mass, radius and metallicity, we may be able to constrain the formation history of a giant planet.

## 4 LHD SIMULATIONS OF GIANT IMPACTS AND MERGERS OF THE GAS GIANTS

Hydrodynamic simulations of GIM can only last for a few dynamic timescales. After the establishment of hydrostatic equilibrium, the giant planet undergoes thermal evolution on a timescale

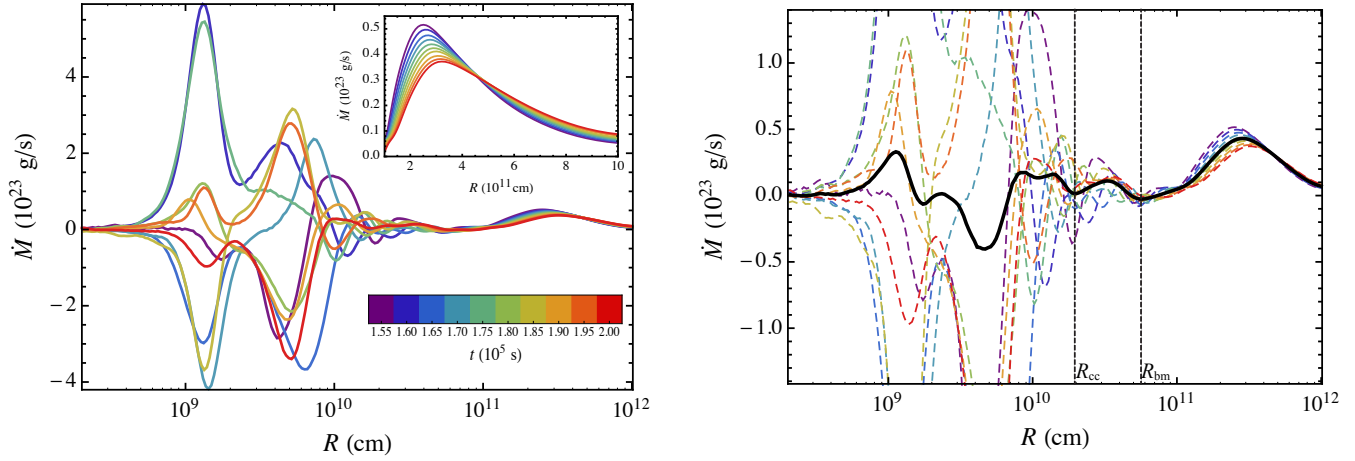


**Figure 5.** Snapshots of mass flux  $\dot{M}$  as a function of radius taken from the FLASH simulation FC1b. In the left panel, different snapshots are plotted in colored lines. We zoom in the outflow region in the subplot. In the right panel, we plot the time-averaged  $\dot{M}$  in black thick line and the colored dashed lines are the snapshots. Two vertical black dashed lines indicate the positions of contiguous radius  $R_{cc}$  and bound radius  $R_{bm}$ , respectively.

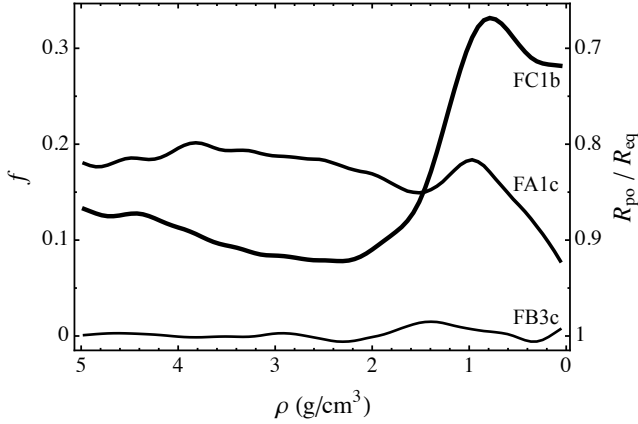


**Figure 6.** Oblateness  $f$  of isodensity surfaces in three FLASH simulations FA1c, FB3c and FC1b. The right-y axis is linearly scaled to show the corresponding  $R_{po}/R_{eq}$  value.

much longer than the dynamical timescale. Here we following the long-term thermal evolution of the remnant gas giant using a one-dimensional Lagrangian Hydrodynamic (LHD) model (see Paper I for model details). Combinations of SPH impact models and 1-D long-term thermal models have been used to examine the luminosity and core-accretion of gas-giants (Broeg & Benz 2012) and long-term luminosity of gas giants (Anic, Alibert & Benz 2007). The details of our one-dimensional LHD model are described in paper I. Here we use similar initial models ( $M_{tot} = 100 M_{\oplus}$ ,  $M_{core} = 10 M_{\oplus}$ ,  $R_{tot} = 7 \times 10^9$  cm,  $R_{core} = 2.2 R_{\oplus}$ ), but consider impacts into short-period planets and calculate models with a much larger range of  $v_{imp}$ . In order to take into account the host stars' tidal potential, we adopt a prescription for the gravitation potential (see §3 in Paper I). In most LHD models presented here, we set the semi major axis of the planet to be at  $a = 0.042$  AU and calculate  $R_R$  ( $\sim 3 \times 10^{10}$  cm =  $4.3 R_J$ ) with  $M_a$  being that of HD 149026 (*i.e.*  $1.3 M_{\odot}$ ). We take the stellar irradiation into account by assuming the surface temperature of the planet to be 1500 K. For comparison, we also simulate other models (LB3e, LA3a, LA3b, LC2a, LC2b) in which, we place the

gas giant at  $a = 0.1$  and 5 AU respectively. The planet's surface temperature is changed accordingly.

#### 4.1 LHD models of GIMs on to hot Jupiters

In this series of simulations, we adopt the same model parameters which we used to simulate head-on collisions with the SPH method. The results of 9 sets of simulations are summarized in Table 4. They are three sets of models in which the impactor is a Saturn-mass gas giant, a  $25 M_{\oplus}$  and a  $10 M_{\oplus}$  embryo. All of the initial models are assumed to be in hydrostatic equilibrium prior to the impact. At the onset of the simulation, in order to take into account the impact energy released in the vicinity of the core, we impose a burst of thermal energy,  $E_a = M_I v_{imp}^2 / 2$ , so that the total energy becomes  $W' = E_a + E_g / 2$ . We also adopt the assumption that cores and embryos are completely merged during head-on impacts. This assumption is supported by the results of SPH models SA1a-SA3a, SB1a-SB4a, and SC1a-SC4a.

For an impactor with  $M_I = 25 M_{\oplus}$ , a parabolic collision (model LA1) leads to a merger without any loss of gaseous envelope. The gas giant's photospheric radius expanded slightly. For a higher-speed collision (model LA2), the envelope expands by a larger factor. Although it is now comparable to some of the inflated transiting planets, this gas giant will contract as it loses its internal energy on a Kelvin Helmholtz time scale. For a hyperbolic encounter (model LA3), the total energy  $E_a$  deposited into the gas giant is comparable to its total gravitational potential energy  $E_g$  prior to the collision. With a positive total energy after the impact ( $W' > 0$ ), the gas giant's envelope expands and disintegrates rapidly.

Analogous dynamical parameters are imposed for a  $10 M_{\oplus}$  impactor. In these models, the final  $R_f$  is slightly smaller for the same impact velocity compared with those models impacted by a larger impactor ( $25 M_{\oplus}$ ). Still, we find total loss of the gaseous envelope in the model (LB3) with high velocity impact.

For the gas giant merger models, LHD simulations yield greater loss of the gaseous envelope. In the low-velocity parabolic model LC1, the merger produces a much larger photospheric radius than the gas giants' initial size. Nevertheless, the entire envelope is

Model	$M_1$	$M_{1,c}$	$v_{\text{imp}}/v_{\text{esc},2}$	$M_{f,c}$	$M_{f,g}$	$M_{f,g}^S$	$R_f/R_i$	$R_f/R_S$	Model	$v_{\text{imp}}/v_{\text{esc},2}$	$a$ (AU)	$\rho_\infty$ $\text{g cm}^{-3}$	$M_{f,c}$ ( $M_\oplus$ )	$M_{f,g}$ ( $M_\oplus$ )	$R_f/R_i$	$R_f/R_S$
LA1	25	25	1.0	35	90	90	1.08	1.25	SB3a	3	—	0.5	20	80.5	1.06	1.05
LA2	25	25	1.4	35	90	88	1.22	1.42	LB3	3	0.042	free	20	0	-	-
LA3	25	25	3.0	35	0	53	-	-	LB3c	3	0.042	$2 \times 10^{-5}$	20	0	-	-
LB1	10	10	1.0	20	90	90	1.10	1.28	LB3d	3	0.042	$5 \times 10^{-3}$	20	0	-	-
LB2	10	10	1.4	20	90	90	1.12	1.30	LB3e	3	0.042	$5 \times 10^{-2}$	20	90	2.80	3.25
LB3	10	10	3.0	20	0	81	-	-	LB3a	3	0.1	free	20	90	2.38	2.61
LC1	100	10	1.0	20	180	180	1.94	2.25								
LC2	100	10	1.4	20	0	180	-	-								
LC3	100	10	3.0	20	0	92	-	-								

**Table 4.** LHD models of collisions of a  $100 M_\oplus$  hot Jupiter with a  $25 M_\oplus$  embryo, a  $10 M_\oplus$  embryo, and another identical gas giant. Each gas giant has a  $10 M_\oplus$  core. In all of these models, the semi major axis of the hot Jupiter is set to be 0.04 AU. All the symbols are identical to previous tables. For each model, we list the asymptotic mass  $M_{f,g}^S$  of remaining gas envelope of the merger product obtained with the SPH simulations (see Tables 1, 2, and 3).

retained due to a comparable increase in the merger’s thermal and gravitational binding energy. The new Roche lobe of the merger is also enlarged so that  $R_f$  remains well inside  $R_R$ . However, with a slightly larger impact speed (model LC2), the thermal energy dissipated is adequate to enlarge  $R_f$  beyond the new  $R_R$ . Outflow across  $R_R$  leads to runaway mass loss.

The results in this subsection indicate a bimodal distribution of GIM outcomes. With high impact speeds, gas giants lose their envelope entirely. Shortly after modest-speeds, gas giants retain their enlarged envelopes. It is possible that subsequent tidal evolution can lead to additional heating and modest mass loss (Gu, Lin & Bodenheimer 2003; Gu, Bodenheimer & Lin 2004). This process can account for the smaller observed masses for hot Jupiters versus long-period gas giants. But it cannot produce intermediate-mass (with  $20M_\oplus < M_p < 100M_\oplus$ ) hot Jupiters in a prolific manner. Thus, the bimodal mass distribution of planets anticipated by planetary synthesis simulations (Ida & Lin 2008; Ida, Lin & Nagasawa 2013) is likely to be preserved despite the high probability of GIMs in the stellar proximity (see §2).

## 4.2 Comparisons between the SPH and LHD models

Similar to the results obtained from LHD calculations, the SPH models in §3 clearly demonstrate a sharp transition between GIMs without much mass loss and total disruption. Modest events hardly modify gas giant’s radius whereas highly energetic GIMs can lead to their total dispersal. However, for some models, LHD calculations generate more significant mass loss after the impact compare with SPH results. This may be caused by the artefact of a density lower limit ( $\rho_l = 0.5 \text{ g cm}^{-3}$ ) which we have adopted for the SPH scheme (see Paper I). While the LHD scheme uses a freely expanding outer boundary condition.

In this subsection, we carry out a series of models to demonstrate how the mass loss rate may depend sensitively on the outer boundary condition (see Table 5). We choose the parameters for an intermediate model SB3a to highlight the difference between SPH and LHD simulations in marginal cases. In the SPH simulations, nearly 90% of the envelope’s original mass was retained after a Saturnian gas giant was impacted by a  $10 M_\oplus$  embryo during a head-on high-speed collision.

**Table 5.** Comparison of LHD models with a SPH model of collisions between a  $100 M_\oplus$  gas giant planet and a  $10 M_\oplus$  embryo. All models in this table are computed for  $v_{\text{imp}} = 3v_{\text{esc},2}$ . In the SPH model, we consider the gas giant in isolation. In LHD models, tidal effect of a  $1.3 M_\odot$  host star is taken into account. For the LHD models, various outer boundary conditions are imposed to demonstrate the numerical artefacts introduced by the lower limit on the external density assumed in the SPH scheme. For the LHD models, the final mass of envelope is computed to be that inside the Roche radius  $R_R$  and the quantity  $R_f$  refers to the photospheric radius when the post-impact expansion of the planetary envelope is stalled.

LHD simulations suggest there may be substantial mass loss associated with this set of parameters. In model LB3 (and most models), the pressure at outer boundary of the planet has a smooth transition from the planetary surface to the disk. The evolution of the density distribution  $\rho$  (at four epochs) after the impact is plotted on the left panel of Figure 7. Due to the dissipation of impactor’s kinetic energy, thermal energy is released near the core. A jump in the pressure drives a rapid initial expansion of the envelope (at around  $5 \times 10^5 \text{ s}$ ). Due to the  $PdV$  work, the expansion speed gradually decreases below the sound speed. Nevertheless, gas in the envelope is able to reach  $R_R$  (where the gravitational potential has a local maximum) with a modest density ( $\rho_R \sim 10^{-4} \text{ g cm}^{-3}$ ) at  $\sim 10^6 \text{ s}$  after the impact. Gas outside  $R_R$  is accelerated outward by the tidal force of the central star with a flux  $\dot{M}_{\text{out}} \sim 4\pi\rho_R R_R^2 v_g > 10^{23} \text{ g s}^{-1}$ . Gas depletion just beyond  $R_R$  reduces the local pressure and a negative pressure gradient drives an outward gas flow to replenish that region. Since  $R_R$  is proportional to  $M_p(R_R)$ , mass loss also decreases the size of  $R_R$ . A continuous flow across  $R_R$  leads to the eventual loss of the entire envelope.

There are some differences in the results in models LB3 and SB3a. Although the same model parameters are used, these two models are computed with LHD and SPH methods respectively. In order to account for these differences, we modify the outer boundary condition such that the planet is assumed to be surrounded by an external medium with a density  $\rho_\infty$  and a temperature  $T = 1,500 \text{ K}$ . We impose a passive external density  $\rho_\infty$  which is set to be  $2 \times 10^{-5}$ ,  $5 \times 10^{-3}$ ,  $5 \times 10^{-2} \text{ g cm}^{-3}$  for models LB3c, d, and e respectively (This external material does not accumulate beyond the planet as it expands). The results in Table 5 indicate that, with sufficiently high  $\rho_\infty$ , expansion of the envelope can be stalled before it reaches  $R_R$ . On the right panel of Figure 7, we plot the initial and stalled density distribution for models LB3d and LB3e. In both models LB3d and LB3e, the external density (or pressure) has stalled the expansion of the envelope. The main difference is that in model LB3d, the envelope continues to expand beyond  $R_R$  whereas in model LB3e, it is stalled and falling back inside  $R_R$ . Due to the outward-directed tidal force, gas outside  $R_R$  does not return to the gas giant. In contrast, the build-up of a dense shell just inside  $R_R$  (in model LB3e) will settle back to the core region. However, the time scale for the dense shell to resettle onto a point mass potential may be larger than the local

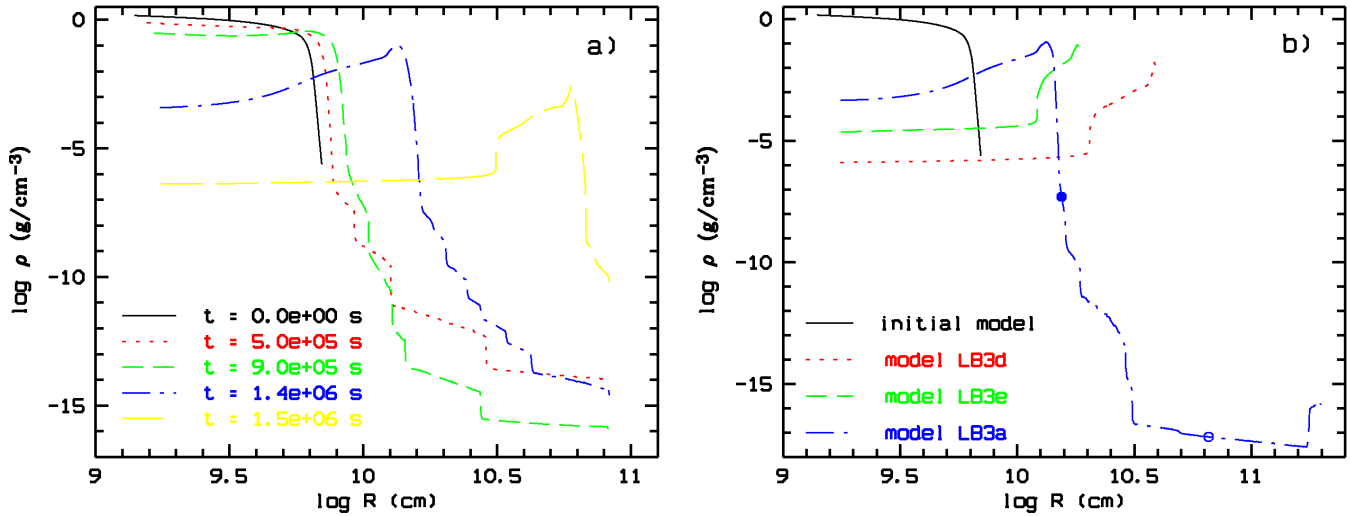


**Figure 7.** Models' density profiles. Left panel: Evolution of the density distribution at different epochs for the model LB3. Right panel: Comparison of the density distributions for models with different boundary conditions.

dynamical time scale, because the magnitude of gravity near  $R_R$  is reduced by the host star's tidal force. The approximate agreements suggest that our adopted value of  $\rho_1$  in the SPH simulations can suppress the effect of envelope's mass loss, especially for marginally disruptive models.

In all SPH models,  $a$  and  $R_R$  are set to be infinite. It is therefore not unfavorable for any gas giant to lose a substantial fraction of its envelope unless GIM's occur with a kinetic energy which at least exceeds its initial gravitational binding energy. Some of the hyper-velocity models do have adequate kinetic energy to disintegrate the gas giant planets. Despite the detachment and high velocity of disposal of a part (but not all) of gas in the original envelopes, a residual amount of gas falls back to re-establish a much reduced envelope (see models SC4a-e). The LHD calculations take into account the stellar tide. When the gaseous envelope of the planet expands beyond its  $R_R$  after the GIM, the gas outside  $R_R$  would not return back to the planetary surface due to the stellar gravity. Therefore, the change of planets'  $a$  (and accordingly  $R_R$ ) should have influences on the retention efficiency of the planetary atmosphere after the impact. We calculate marginal models with different  $a$ 's and  $R_R$ 's and present comparisons in the subsection below.

### 4.3 GIM's on to intermediate and long-period gas giants

We have shown in our LHD models that in the stellar proximity where hot Jupiters'  $R_R$  is only a few times Jovian radii, energetic GIM's lead to catastrophic loss of their gaseous envelopes. During some GIM's (such as those in models LA3 and LB3), although the initial expansion of a gas giant's gaseous envelope's is stalled with its  $R_f$  interior to  $R_R$ , there is sufficient density at  $R_R$  to enable a high outflow flux. In these marginal cases, it is natural to explore whether a fraction of the initial envelope may be retained in the limit of larger  $R_R$ 's. Take model LB3 for example, the total kinetic energy carried by the impactor is comparable to half of the total gravitational binding energy of the pre-impact gas giant. In the limit of negligible stellar tide, we anticipate that the planet's enve-

lope may double its half mass radius and increases the photospheric radius to even larger extent.

The magnitude of  $R_R$  increases with  $a$ . Since gas giants probably formed outside the snow line at a few AU's from their host stars (Ida & Lin 2004), their  $R_R$  is two orders of magnitude larger than that of the hot Jupiters. In order to explore dependence of the envelope retention on the tidal perturbation of the host star, we consider variations of models LA3 and LB3 in which  $a$  is chosen to be 0.1 AU and 5 AU. The surface temperature of these models are set to be 1000 K and 150 K accordingly. We list the models parameters and results in Table 6.

In the choice of these model parameters, the target Saturn-mass gas giant had  $v_{\text{esc}} = 25 \text{ km s}^{-1}$  while the Keplerian speeds at 0.1 and 5 AU around HD 149026 are  $> 100 \text{ km s}^{-1}$  and  $\sim 15 \text{ km s}^{-1}$  respectively. Although it is possible for GIM's to occur with  $v_{\text{imp}} = 3v_{\text{esc},2}$  at 0.1 AU (models LA3a and LB3a), it is highly unlikely for  $v_{\text{imp}}$  to be much larger than  $v_{\text{esc},2}$  at 5 AU (in models LA3b and LB3b). Therefore, the simulation of highly energetic GIM's onto long-period exoplanets should be considered theoretical toy models albeit they can also be used to represent GIM's by more massive super-Earths with somewhat smaller  $v'_{\text{imp}}$ 's.

The total energy deposited during a hyper-velocity impact in the hot-Jupiter model LB3 is around half of the gas giant's initial gravitational binding energy or comparable to its total energy. In principle, gas giant's envelope should be more than double after it is fully virialized, which is consistent with our FLASH simulations. However,  $R_R$  for this hot Jupiter is only five times  $R_p$  prior to the impact. The initial expansion overshoot causes sufficiently dense ( $\rho > 10^{-5} \text{ g cm}^{-3}$ ) outer region of the envelope to extend outside the gas giant's Roche lobe such that it leads to rapid mass loss. In model LB3a, however, both  $a$  and  $R_R$  are set to be more than twice as large as their values in model LA3. Consequently, the envelope expansion is stalled well inside  $R_R$  with very little mass loss. At later stages, the envelope contracts slightly as a quasi hydrostatic equilibrium is re-established while the radius of the photosphere is doubled from its pre-impact value. For comparison, we overplotted the stalled density profile of this model on the right panel of Figure

7. In order to demonstrate the locations of planetary photosphere and Roche radius after the GIM, we marked them with filled and open circles respectively. We also consider a model located at larger value of  $a$  ( $= 5$  AU). In this case, the gaseous envelope is still well preserved.

For the models LAa and LCa, the Roche lobe is still sufficiently compact, that there is considerable outflow and depletion of the gas envelope. In long-period models (LAb and LCb), the  $R_R$ 's are so large that the expanding envelopes can hardly reach them. Even though, the gaseous envelopes in these models are dispersed as their expanding velocities have already exceeded the escape velocity.

The total thermal energy input  $E_a$  (or kinetic energy dissipation) at the onset of these two models is comparable to the initial gravitational binding energy of the gas giant  $E_g$ . Consequently, the net total energy ( $W'$ ) is slightly positive. During the initial expansion, this newly added internal energy is converted into a self-similar outflow everywhere analogous to the Sedov-Taylor solution for supernova explosions. In the absence of energy losses, the magnitude of the gravitational binding energy would reduce with that of the internal energy while there would be adequate kinetic energy to disintegrate the entire envelope with an outflow velocity  $\sim (2W'/M_p)^{1/2}$ .

In the limit that sufficient thermal energy is deposited into these long-period gas giants, it is possible for a fraction of the envelope be dispersed while the rest is retained around the merged core. During the expansion of the gaseous envelope after an energetic impact, a fraction of the envelope remains around the core, albeit the asymptotic photosphere  $R_f$  is more than doubled. The radius of the photosphere  $R_f$  cannot expand indefinitely because the column density along the radial direction decreases with the expansion of the gas giant. For self-similar expansions, the total opacity of the gaseous envelope is  $\tau_{\text{tot}} \propto R_{\text{exp}}^{-2}$  where  $R_{\text{exp}}$  is an expansion factor. For sufficiently large  $R_{\text{exp}}$ , the envelope becomes optically thin and the total energy can no longer be conserved. Rapid radiative loss can reduce  $W'$  below zero. This transition is equivalent to that from Sedov to snowplough phase of supernova shells. The envelope would be totally disrupted if  $W'$  is sufficiently large that at the transition phase, the outflow has already acquired a velocity in excess of the escape speed. Otherwise, a fraction of the envelope may be retained in the form of “fall back” gas.

Our models indicate that partial retention of a gas giant's envelope after a giant embryo impact requires a narrow range of energy deposition. This energy is generally unattainable from embryos and super-Earths near the sites of gas giant formation. Thus the mass of long-period gas giants is generally retained while their heavy elemental content is being enriched by GIM's.

#### 4.4 De-synchronization of the envelope and further inflation

If a state of spin-orbit synchronization has already been accomplished by tidal evolution prior to the giant impact, both off-center collisions and the expansion of the envelope would introduce asynchronous spin and perhaps modest orbital eccentricity in general. As an example, we simulate in model SC1b, the merger event of two identical planets during which their cores also coalesce. Although the envelope experienced a more significant expansion, most of the envelope remains intact. In this case, the final spin rate would differ substantially from its initial values. This departure from synchronous rotation may have observable consequences

for atmospheric flows (Rauscher & Kempton 2014) and thermal evolution.

Subsequent tidal dissipation would lead to an additional source of heating for the planet (Dobbs-Dixon, Lin & Marling 2004) such that

$$\dot{E}_t = \frac{GM_* M_p e_p^2}{a(1 - e_p^2)\tau_e} + \frac{\alpha_p M_p R_p^2 (n_p - \Omega_p)^2}{\tau_\Omega}, \quad (13)$$

where  $\tau_\Omega = (7\alpha_p/2)(R_p/a)^2\tau_e$  is the synchronization time scale and  $\tau_e$  is the eccentricity damping time scale. The rate of energy dissipation depends not only on the differential angular frequency but also on the radius and internal core-envelope structure of the planet through its  $Q'_p$  value (Ogilvie & Lin 2004). Although the amount of extractable energy in the planet's spin is limited, for a brief duration  $\tau_\Omega$ , the rate of tidal dissipation due to synchronization is comparable to that due to circularization. Under some circumstances, the planet's envelope would further expand and perhaps overflow its Roche lobe, if the tidal dissipation rate exceeds the energy loss rate at the planet's surface (Gu, Lin & Bodenheimer 2003; Gu, Bodenheimer & Lin 2004). We shall present an analysis of this possibility elsewhere.

#### 4.5 Consequence of giant impacts on HD 149026

Based on the results of the previous subsections, we propose the progenitor of HD 149026b formed with a Saturn-like internal structure. When it migrated to the proximity of its host star, it may have merged with another short-period gas giant or a population of close-in super earths. If these collisions occurred with relatively low impact speeds, phase transition of the core material would be avoided. Nevertheless, heavy elements in the core would mix with an inflated envelope. Subsequent tidal evolution provides additional heating which may have led to the partial loss of its gaseous envelope through Roche-lobe overflow. We note that HD 149026b is less massive than most known hot Jupiters and could have lost some mass. The metal-rich debris material would stream into the host star and significantly increase the metallicity of its shallow outer envelope (Li, Lin & Liu 2008). Angular momentum transfer between the planet and the debris stream would also enlarge the planet's orbital semi major axis and Roche lobe so that the envelope loss would be limited. On a time scale comparable to the age of its host star, this planet would contract to its present-day radius.

We anticipate common occurrence of similar type of merger events. Since it is difficult to assess the optimum initial conditions for this model, we now present a series of simulations with a HD 149026b-like planet as our initial model. The total mass of the initial model is  $110-M_\oplus$ , and the core mass is around  $73-M_\oplus$ . According to the observations of HD 149026b (Sato et al. 2005), the initial model has  $R_p = 0.73R_J$ ,  $a = 0.042$  AU, and  $T_e = 1500$  K accordingly.

We calculate models struck by embryos with different masses and speeds. The model parameters and results are listed in Table 7. For the models struck by a  $10-M_\oplus$  or a  $25-M_\oplus$  embryo with low speed ( $v_{\text{imp}}/v_{\text{esc},2} = 1.0$ ), there is still inflation of its gaseous envelope. For larger impact velocity  $v_{\text{imp}}/v_{\text{esc},2} = 1.4$ , the gaseous envelope of the model impacted by  $25-M_\oplus$  embryo has already expanded beyond its  $R_R$ .

When comparing the two series of models (Saturn-like and HD 149026b-like models), we find that Saturn-like models are

Model	$M_1$ ( $M_{\oplus}$ )	$M_{1,c}$ ( $M_{\oplus}$ )	$a$ (AU)	$v_{\text{imp}}/v_{\text{esc},2}$	$M_{f,c}$ ( $M_{\oplus}$ )	$M_{f,g}$ ( $M_{\oplus}$ )	$R_f/R_i$	$R_f/R_S$
LA3	25	25	0.04	3.0	35	0	-	-
LA3a	25	25	0.1	3.0	35	0	-	-
LA3b	25	25	5.0	3.0	35	0	-	-
LB3	10	10	0.04	3.0	20	0	-	-
LB3a	10	10	0.1	3.0	20	90	2.38	2.61
LB3b	10	10	5.0	3.0	20	90	1.68	1.73
LC2	100	10	0.04	1.4	20	0	-	-
LC2a	100	10	0.1	1.4	20	0	-	-
LC2b	100	10	5.0	1.4	20	0	-	-

**Table 6.** Comparisons of LHD models at different semi-major axes. The impacted model is a  $100 M_{\oplus}$  gas giant with a  $10 M_{\oplus}$  core. All the symbols are identical to the previous tables.

more resilient in retaining the gas envelope during the impacts. Even though some of the Saturn-like models (LA2) are hit by impactor with masses several times greater than that in the catastrophic HD 149026b-like model LB2S, there is no significant mass loss in these models. This dichotomy may be explained by the following reasons. In the calculations, we assume that all the impactors can reach the core, with ablated mass and gravitational energy deposited in a region around the core. Thus, the deposited energy by the impactor is not only function of the mass, but also related its path and the internal structure of the target. For the same amount of material deposited at the same location, the deposited energy would be larger in the HD 149026b-like models than that in the Saturn-like models, because the former have much larger solid core than the latter. And a side effect of the massive impactors is that the Hill radius will increase with the increasing mass of impactor, which will make it more difficult for the envelope to expand out of its Hill radius. Furthermore, the Saturn-like models have very massive gaseous envelope compared with the HD 149026b-like models. They obviously require much larger energy deposition to overcome the gravitational binding for the envelope to escape out of the Hill radius.

## 5 SUMMARY AND DISCUSSIONS

### 5.1 A brief summary

During the formation and dynamic evolution of the planetary system, there are many avenues of GIMs by embryos onto hot Jupiters. The supply of these large solid building blocks includes: 1) planetesimals along the paths of migrating gas giants, 2) super-Earths stalled at barriers outside the asymptotic destiny of hot Jupiters, 3) terrestrial bodies cleared by sweeping secular resonances and dynamical instabilities, and 4) short-period super Earths subjected to tidal orbital evolution.

There are also several processes which can lead to the merger of gas giants: 1) orbit crossing triggered by run-away migration, 2) congregation of hot Jupiters near their host stars, and 3) long-term dynamical instability in the stellar proximity.

Based on these consideration and the observation that a large fraction of stars bear super-Earths and a large fraction of known gas giants are members of multiple-planet systems, we infer common occurrence of close encounters among these relatively massive gaseous and solid planets. These events can lead to the observed

Rayleigh distribution of gas giants' orbital eccentricity (Zhou, Lin & Sun 2007; Jurić & Tremaine 2008; Chatterjee et al. 2008).

### 5.2 Potential outcomes of GIM events

Here, we suggest that some of these close encounters results in GIMs. The energy released during such collisions may lead to expansion of the planets' envelope. If this GIM scenario is applicable for the origin of the exceptional inflated close-in planets, their fraction (relative to the normal-size planets) would correspond to the duty cycle of a planet's expanded state following a major impacting event. On the Kelvin-Helmholtz time scale ( $\sim 10^8$  yr), the inflated planets return to their initial state of thermal equilibrium.

Under the assumption that the residual planetesimals and embryos are sufficiently depleted that their characteristic collision time scale with close-in gas giants is comparable to the age of their host stars, the population of inflated planets is expected to be an order of magnitude less than that of the normal size gas giants. This inference is consistent with the relatively small fraction of inflated to normal close-in gas giants.

In the proximity of their host stars, a substantial amount of the envelope gas may be lost, after each giant impact, through Roche-lobe overflow (Gu, Bodenheimer & Lin 2004), leading to a large metallicity enhancement of the planets. The intermediate-mass merger products may account for a population of planets found in the "planetary desert" which was predicted by the population synthesis models (Ida & Lin 2004; Howard et al. 2010; Ida, Lin & Nagasawa 2013). The metal-rich planetary debris may also be accreted by their host stars, leading to modest enrichment of the stellar outermost envelope (Li, Lin & Liu 2008). These events of planetary coalescence and the pollution of their host stars are unlikely to occur if gas giants are formed through gravitational instability. The verification of this GIM scenario may provide a distinguishing test for these competing scenarios of planet formation.

For planet with longer orbital periods, tidal evolution toward spin synchronization is weak, angular momentum deposited by impacts can be reserved. In the future, oblateness measurements may be used to constrain impact history of gas giant planets.

### 5.3 HD 149026b

In this paper, we considered the possibility that the large core of hot Jupiter, HD 149026b formed through giant impacts onto a gas giant planet with either residual proto-planetary embryos or merger

Model	$M_1$ ( $M_\oplus$ )	$M_{1,c}$ ( $M_\oplus$ )	$v_{\text{imp}}/v_{\text{esc},2}$	$M_{f,c}$ ( $M_\oplus$ )	$M_{f,g}$ ( $M_\oplus$ )	$M_{f,g}^N$ ( $M_\oplus$ )	$R_f/R_i$	$R_f/R_S$
LA1S	25	25	1.0	98	37	90	2.00	1.76
LA2S	25	25	1.4	98	0	90	-	-
LA3S	25	25	3.0	98	0	0	-	-
LB1S	10	10	1.0	83	37	90	1.13	1.00
LB2S	10	10	1.4	83	37	90	1.47	1.29
LB3S	10	10	3.0	83	0	0	-	-

**Table 7.** LHD models of HD 149026b-like planet impacted by embryos with different masses. The initial model has a total mass of  $110 M_\oplus$  and a  $73 M_\oplus$  core. In all of these models, the semi major axis of the impacted planet is set to be 0.042 AU. The results for collisions onto Saturn-like planet are also listed as  $M_{f,g}^N$  for comparison.

with other gas giant planets in the proximity of its host star. In order to examine the outcome of these collisions, we carried out a series of numerical simulations with a SPH algorithm. These calculations demonstrate gentle collisions always lead to coalescence whereas nearly parabolic direct collisions can result in a preferential loss of gaseous envelope material while the heavy elements in the core are mostly retained. But, most of the core material may not merge or be retained as a consequence of oblique high-velocity collisions.

We assume that a substantial fraction of the original residual planetesimals in the neighborhood of HD 149026b may have been scattered into its host star which is an F star with a very shallow convective layer. We carried out evolution calculations to take into account of the effect of stellar pollution. We suggest that in this and other F star with planets, the extent of stellar pollution by residual planetesimals may be tested by an accurate determination of their mass, luminosity, and effective temperature. Such a determination will provide a firm support on the once existence of terrestrial-planet-building material.

#### ACKNOWLEDGMENTS

We thank Drs F. Adams, E. Asphaug, P. Bodenheimer, J. Guillochon, T. Guillot, Y. Hori, S. Ida, M. Kouwenhoven and G. Laughlin for useful conversations. We also thank the referee David Stevenson for constructive comments. The software used in the hydrodynamic simulations was in part developed by the DOE-supported ASCI/Alliance Center for Astrophysical Thermonuclear Flashes at the University of Chicago. Computations were performed on the Laohu computer cluster at NAOC and the Hyades clusters at UCSC. This work is supported by UC/Lab Fee grants. S.-F. L. was sponsored by NASA NNX13AR66G "Collisional Accretion of Similar Sized Bodies". This work is also supported by the Astronomy Unit's STFC Consolidated Grant.

#### REFERENCES

- Adams F. C., Laughlin G., 2001, *Icarus*, 150, 151  
Agnor C., Asphaug E., 2004, *ApJ*, 613, L157  
Agnor C. B., Lin D. N. C., 2012, *ApJ*, 745, 143  
Anderson K. R., Adams F. C., 2012, *PASP*, 124, 809  
Anic A., Alibert Y., Benz W., 2007, *A&A*, 466, 717  
Asphaug E., Agnor C. B., Williams Q., 2006, *Nat*, 439, 155  
Baraffe I., Chabrier G., Barman T., 2008, *A&A*, 482, 315  
Barnes J. W., Fortney J. J., 2003, *ApJ*, 588, 545  
Batygin K., Stevenson D. J., 2010, *ApJ*, 714, L238  
Benz W., Slattery W. L., Cameron A. G. W., 1986, *Icarus*, 66, 515  
Bodenheimer P., Laughlin G., Lin D. N. C., 2003, *ApJ*, 592, 555  
Bodenheimer P., Lin D. N. C., Mardling R. A., 2001, *ApJ*, 548, 466  
Boss A. P., 1997, *Science*, 276, 1836  
Broeg C. H., Benz W., 2012, *A&A*, 538, A90  
Burrows A., Guillot T., Hubbard W. B., Marley M. S., Saumon D., Lunine J. I., Sudarsky D., 2000, *ApJ*, 534, L97  
Burrows A., Hubeny I., Hubbard W. B., Sudarsky D., Fortney J. J., 2004, *ApJ*, 610, L53  
Canup R. M., 2008, *Icarus*, 196, 518  
Canup R. M., Barr A. C., Crawford D. A., 2013, *Icarus*, 222, 200  
Chatterjee S., Ford E. B., Matsumura S., Rasio F. A., 2008, *ApJ*, 686, 580  
Dobbs-Dixon I., Lin D. N. C., Mardling R. A., 2004, *ApJ*, 610, 464  
Faber J. A., Rasio F. A., Willems B., 2005, *Icarus*, 175, 248  
Fabrycky D., Tremaine S., 2007, *ApJ*, 669, 1298  
Fogg M. J., Nelson R. P., 2007, *A&A*, 461, 1195  
Freitag M., Benz W., 2005, *MNRAS*, 358, 1133  
Fryxell B. et al., 2000, *ApJS*, 131, 273  
Garaud P., Lin D. N. C., 2007, *ApJ*, 654, 606  
Gillon M. et al., 2007, *A&A*, 466, 743  
Goldreich P., Soter S., 1966, *Icarus*, 5, 375  
Goldreich P., Tremaine S., 1980, *ApJ*, 241, 425  
Gu P.-G., Bodenheimer P. H., Lin D. N. C., 2004, *ApJ*, 608, 1076  
Gu P.-G., Lin D. N. C., Bodenheimer P. H., 2003, *ApJ*, 588, 509  
Guillochon J., Ramirez-Ruiz E., Lin D., 2011, *ApJ*, 732, 74  
Howard A. W. et al., 2010, *Science*, 330, 653  
Hui L., Seager S., 2002, *ApJ*, 572, 540  
Ida S., Lin D. N. C., 2004, *ApJ*, 604, 388  
Ida S., Lin D. N. C., 2008, *ApJ*, 685, 584  
Ida S., Lin D. N. C., Nagasawa M., 2013, *ApJ*, 775, 42  
Ikoma M., Guillot T., Genda H., Tanigawa T., Ida S., 2006, *ApJ*, 650, 1150

- Jurić M., Tremaine S., 2008, *ApJ*, 686, 603
- Ketchum J. A., Adams F. C., Bloch A. M., 2011, *ApJ*, 741, L2
- Kippenhahn R., Weigert A., Weiss A., 2013, *Stellar Structure and Evolution*. Springer-Verlag, Berlin
- Kretke K. A., Lin D. N. C., 2012, *ApJ*, 755, 74
- Laughlin G., Adams F. C., 1998, *ApJ*, 508, L171
- Lee M. H., Fabrycky D., Lin D. N. C., 2013, *ApJ*, 774, 52
- Lee M. H., Peale S. J., 2002, *ApJ*, 567, 596
- Leinhardt Z. M., Stewart S. T., 2012, *ApJ*, 745, 79
- Li S. L., Agnor C. B., Lin D. N. C., 2010, *ApJ*, 720, 1161
- Li S.-L., Lin D. N. C., Liu X.-W., 2008, *ApJ*, 685, 1210
- Li S.-L., Miller N., Lin D. N. C., Fortney J. J., 2010, *Nat*, 463, 1054
- Lin D. N. C., Bodenheimer P., Richardson D. C., 1996, *Nature*, 380, 606
- Lin D. N. C., Ida S., 1997, *Astrophysical Journal* v.477, 477, 781
- Lin D. N. C., Papaloizou J. C. B., Kley W., 1993, *ApJ*, 416, 689
- Liu S.-F., Guillochon J., Lin D. N. C., Ramirez-Ruiz E., 2013, *ApJ*, 762, 37
- Mandell A. M., Raymond S. N., Sigurdsson S., 2007, *ApJ*, 660, 823
- Mandushev G. et al., 2007, *ApJ*, 667, L195
- Marchi S., Ortolani S., Nagasawa M., Ida S., 2009, *MNRAS*, 394, L93
- Marcus R. A., Stewart S. T., Sasselov D., Hernquist L., 2009, *ApJ*, 700, L118
- Mardling R. A., 2007, *MNRAS*, 382, 1768
- Mardling R. A., Lin D. N. C., 2004, *ApJ*, 614, 955
- Melosh H. J., 1989, *Impact cratering: A geologic process*. Oxford Univ. Press, New York
- Murray N., Holman M., 1999, *Science*, 283, 1877
- Nagasawa M., Ida S., 2011, *ApJ*, 742, 72
- Nagasawa M., Ida S., Bessho T., 2008, *ApJ*, 678, 498
- Nagasawa M., Lin D. N. C., 2005, *ApJ*, 632, 1140
- Nagasawa M., Lin D. N. C., Thommes E., 2005, *ApJ*, 635, 578
- Narita N. et al., 2007, *Publ. Astron. Soc. Japan*, 59, 763
- Novak G. S., Lai D., Lin D. N. C., 2003, in *Astronomical Society of the Pacific Conference Series*, Vol. 294, *Scientific Frontiers in Research on Extrasolar Planets*, Deming D., Seager S., eds., pp. 177–180
- Ogilvie G. I., Lin D. N. C., 2004, *ApJ*, 610, 477
- Paardekooper S.-J., Baruteau C., Kley W., 2011, *MNRAS*, 410, 293
- Papaloizou J. C. B., Terquem C., 2010, *MNRAS*, 405, 573
- Pollack J. B., Hubickyj O., Bodenheimer P., Lissauer J. J., Podolak M., Greenzweig Y., 1996, *Icarus*, 124, 62
- Rasio F. A., Ford E. B., 1996, *Science*, 274, 954
- Rauscher E., Kempton E. M. R., 2014, *ArXiv e-prints*
- Rosenblum E., Garaud P., Traxler A., Stellmach S., 2011, *ApJ*, 731, 66
- Sasselov D. D., 2003, *ApJ*, 596, 1327
- Sato B. et al., 2005, *ApJ*, 633, 465
- Schlaufman K. C., Lin D. N. C., Ida S., 2009, *ApJ*, 691, 1322
- Seager S., Hui L., 2002, *ApJ*, 574, 1004
- Shiraishi M., Ida S., 2008, *ApJ*, 684, 1416
- Shoemaker E. M., 1962, in *Physics and Astronomy of the Moon*, ed. Z. Kopal (New York: Academic), 283.
- Showman A. P., Guillot T., 2002, *A&A*, 385, 166
- Spurzem R., Giersz M., HEGGIE D. C., Lin D. N. C., 2009, *ApJ*, 697, 458
- Tasker E. J., Brunino R., Mitchell N. L., Michielsen D., Hopton S., Pearce F. R., Bryan G. L., Theuns T., 2008, *MNRAS*, 390, 1267
- Terquem C., Papaloizou J. C. B., 2007, *ApJ*, 654, 1110
- Thommes E., Nagasawa M., Lin D. N. C., 2008, *ApJ*, 676, 728
- Turk M. J., Smith B. D., Oishi J. S., Skory S., Skillman S. W., Abel T., Norman M. L., 2011, *ApJS*, 192, 9
- Ward W. R., 1981, *Icarus*, 47, 234
- Ward W. R., 1984, in *IAU Colloq. 75: Planetary Rings*, Greenberg R., Brahic A., eds., pp. 660–684
- Ward W. R., 1997, *Icarus*, 126, 261
- Weidenschilling S. J., Marzari F., 1996, *Nat*, 384, 619
- Winn J. N. et al., 2007, *ApJ*, 665, L167
- Wolf A. S., Laughlin G., Henry G. W., Fischer D. A., Marcy G., Butler P., Vogt S., 2007, *ApJ*, 667, 549
- Wu Y., Lithwick Y., 2011, *ApJ*, 735, 109
- Wu Y., Lithwick Y., 2013, *ApJ*, 763, 13
- Wu Y., Murray N., 2003, *ApJ*, 589, 605
- Wu Y., Murray N. W., Ramsahai J. M., 2007, *ApJ*, 670, 820
- Yu Q., Tremaine S., 2001, *AJ*, 121, 1736
- Zel'dovich Y. B., Raizer Y. P., 1967, *Physics of shock waves and high-temperature hydrodynamic phenomena*. Academic Press, New York
- Zhou J.-L., Aarseth S. J., Lin D. N. C., Nagasawa M., 2005, *ApJ*, 631, L85
- Zhou J.-L., Lin D. N. C., 2007, *ApJ*, 666, 447
- Zhou J.-L., Lin D. N. C., Sun Y.-S., 2007, *ApJ*, 666, 423